THESIS

FAST 3D RADIATIVE TRANSFER OF SHORTWAVE REFLECTANCE FOR SYNERGISTIC REMOTE SENSING APPLICATIONS

Submitted by

Joe Kelly

Department of Atmospheric Science

In partial fulfillment of the requirements

For the Degree of Master of Science

Colorado State University

Fort Collins, Colorado

Spring 2023

Master's Committee:

Advisor: Christine Chiu

Steven D Miller
Chandra Venkatachalam

ABSTRACT

FAST 3D RADIATIVE TRANSFER OF SHORTWAVE REFLECTANCE FOR SYNERGISTIC REMOTE SENSING APPLICATIONS

Marine stratocumulus clouds are a critical component of Earth's radiation budget and remain a key source of uncertainty in climate projections. Better representing these clouds and their interactions with radiation, precipitation and aerosols in models necessitates observations of three-dimensional (3D) cloud fields. While passive satellite observations provide critical information on cloud properties globally, their retrievals lack information on vertical structure. Most retrieval methods also assume one-dimensional (1D), plane parallel clouds, leading to significant retrieval errors for both stratocumulus and cumulus regimes. In contrast, observations from active sensors allow for the probing of cloud vertical structure. However, active sensor data are limited in coverage. Combining active and passive satellite observations provides an excellent opportunity to reconstruct the 3D cloud fields.

To provide 3D cloud property fields that do not suffer from errors introduced by the plane-parallel assumption, 3D radiative effects must be incorporated during the retrieval process. In this thesis, the impact of 3D radiative effects on 1D retrievals of cloud optical and microphysical properties is quantified, focusing on contrasting illuminated and shadowed pixels. When evaluating 1D retrieval on a synthetic cloud field, it is found that shadowed pixels had a larger magnitude of mean optical depth bias (–12) than illuminated pixels (3) at small solar zenith angles, while shadowed pixels had a lower magnitude of mean optical depth bias (–5) than illuminated pixels (12) at large solar zenith angles. For effective radius, the mean biases in shadowed and

illuminated pixels are respectively 3.9 μm and –4.9 μm at large solar zenith angles. At small solar zenith angles, shadowed pixels had a smaller mean effective radius bias (0.8 μm) than illuminated pixels (–3.8 μm). By incorporating 3D radiative effects into the retrieval of the synthetic cloud field, the range of retrieved optical depth errors is greatly reduced from [–50, 100] to [–30, 40].

In addition to the synthetic dataset, we highlight a real-world case from the Variability of the American Monsoon System (VAMOS) Ocean-Cloud-Atmosphere-Land Study Regional Experiment (VOCALS-REx), serving as a potential dataset for evaluating 1D and 3D retrievals. Cloud microphysical properties were derived from in-situ cloud probe measurements collected from a profiling flight and three longer and horizontal transects that were within 1 hour of the A-Train overpass. In this particular cloud profile, the cloud droplet number concentrations ranged between 100–150 cm^{-3} and were relatively constant with height; cloud liquid water content increased approximately linearly with height, following a sub-adiabatic growth rate of 1.4 g m^{-3} km^{-1}. We have found that properties from three horizontal transects have similar cloud statistics and structures. Applying the retrieval method to real-world data proved challenging due to the limited vertical information available from satellites about clouds near the surface and due to the inherent uncertainties of comparing cloud fields at different times.

Lastly, to incorporate 3D radiative effects in the retrieval process, we have developed 3D shortwave radiative transfer emulators for stratocumulus and cumulus cloud fields using a convolutional neural network. The emulators were trained on cloud fields generated from the Large Eddy Simulation (LES) and specific sets of solar and viewing geometry and aerosol conditions. The performance of emulators was evaluated against a testing dataset in which the truth reflectance was computed by a 3D radiative transfer model with a subset of LES output as the input cloud fields. Overall, the predicted reflectance at the top of the atmosphere in the visible and

near-infrared spectral regions has mean relative errors smaller than 2%, and the 15th and 85th percentile errors are generally less than ±10% for all setups. This type of emulator can be integrated into remote sensing applications and allow 3D radiative effects to be integrated effectively into advanced retrieval methods.

ACKNOWLEDGEMENTS

First and foremost, I'd like to thank my advisor, Prof. Christine Chiu. Through her mentorship, I have learned how to better approach and think about research. Her support and guidance have been invaluable throughout my master's program and the writing of this thesis. Most importantly, my work with Christine through every step of the past two years has caused me to grow as a person and instilled within me a deep appreciation for the research process and the field of atmospheric science.

I would also like to thank my committee members, Prof. Steve Miller and Prof. Chandra Venkatachalam. Their knowledge and expertise have been invaluable. I would like to give special thanks to Steve Miller, whose feedback has substantially improved this thesis.

I also want to give my gratitude to Kevin Yang, a fellow student in the Chiu research group. His help and guidance were indispensable for key aspects of this project, especially for my understanding of machine learning and radiative transfer. His passion for research and radiation is inspiring.

The support which has led me to this point has been more than academic, which is why I would like to thank my family and girlfriend. Their encouragement has motivated me throughout these past two years, giving me the confidence in myself that I needed. Lastly, I'd like to thank the friends I have made in the department who have made Fort Collins feel like a community.

TABLE OF CONTENTS

CHAPTER 1: INTRODUCTION

1.1. Importance of marine boundary layer clouds.

Marine boundary layer (MBL) clouds are a fundamental component of Earth's radiation budget (Hartmann et al., 1992) and remain one of the primary sources of uncertainty in climate projections (e.g., Bony & Dufresne, 2005). MBL clouds can strongly reflect incoming sunlight and have only a small effect on outgoing longwave radiation. Thus, these clouds have a strong negative radiative effect, as their presence causes more radiation to exit the atmosphere than under clear-sky conditions (Wood, 2012). Moreover, low marine clouds regulate the water cycle via precipitation, which can be modulated by ambient aerosol conditions (e.g., Wood, 2012). Increases in anthropogenic aerosol production will affect cloud microphysics and therefore cloud radiative and precipitative properties by increasing the abundance of cloud condensation nuclei, thereby increasing cloud droplet number concentration. This effect increases cloud albedo and increases cloud lifetime by slowing the cloud droplet coalescence rate, delaying or suppressing rainfall, both of which create a negative radiative forcing (e.g., Andreae & Rosenfeld, 2008). Observations of three-dimensional (3D) cloud fields are crucial for advancing our process-level understanding and improving model physics in interactions between MBL clouds, aerosols, precipitation, and radiation.

1.2. Cloud observations

Several platforms for cloud observations exist, including ground-based, in-situ, and satellite observations. Ground-based remote sensing observations can provide high-temporal cloud information and detailed vertical profiles of clouds but are limited to a single location. In contrast, satellite-based observations can provide information on global coverage and be used to retrieve cloud properties. For oceans and remote locations, satellite-based observations can be the only

data source and are thus particularly important (Werkmeister et al., 2015). Unlike remote sensing observations, aircraft in-situ cloud probes directly measure cloud and precipitation size distribution and water content, but have very limited spatial coverage. Even though in-situ observations have a severe limitation in spatial coverage and are typically available only during field campaigns, the statistics derived from those measurements remain invaluable for evaluating models (e.g., Martin et al., 2019) and satellite-based cloud retrievals (Painemal & Zuidema, 2011).

Among these three sources of cloud observations, satellite-based measurements no doubt play a critical role in monitoring clouds globally. Spaceborne sensors can be classified into two types: the first category is active sensors that transmit and receive signals such as radar and lidar, while the second category is passive sensors that receive reflected sunlight and emitted infrared radiation. Active sensors, such as from the CloudSat satellite's Cloud Profiling Radar (CPR; Stephens et al., 2002) and the Cloud-Aerosol Lidar and Infrared Pathfinder Satellite Observation (CALIPSO; Winker et al., 2010) satellite's Cloud-Aerosol Lidar with Orthogonal Polarization (CALIOP), provide vertical cloud locations and properties (Marchand et al., 2008; Vaughan et al., 2009), but this information is only located along a single near-nadir track with limited horizontal coverage. In general, using CPR data to study MBL clouds can be challenging, since reflectivity from surface clutter can be large and contaminate signals of low clouds that are below 1 km (Marchand et al., 2008). While lidar measurements do not suffer this problem so heavily, unfortunately, lidar signals tend to attenuate completely and quickly in MBL clouds. Thus, while lidars are excellent for detecting cloud top they cannot provide detailed information on cloud vertical structure (Pan et al., 2021).

Passive sensors, such as the Moderate Resolution Imaging Spectrometer (MODIS), which operates on the Terra and Aqua satellites, measure radiances that can be used to retrieve

information on cloud optical thickness, cloud-top effective radius, cloud phase, cloud-top temperature and thus cloud top height or pressure. The advantage of passive observations is the extent of their horizontal coverage. For example, MODIS observes a swath of 2330 km at a resolution as fine as 250 m and can view the entire surface of the Earth every one to two days. However, signals received by passive sensors mainly represent properties close to the cloud top and lack information on the full vertical structure of clouds (Platnick et al., 2015).

Over the past decades, many cloud optical and microphysical properties retrieved from satellite shortwave reflectance measurements are based on the so-called "Nakajima-King" diagram, as shown in Fig. 1.1 (Nakajima & King, 1990). This type of retrieval method uses reflectance at two wavelengths, one water-absorbing and one non-absorbing. The non-water-absorbing wavelengths are typically selected from visible bands (e.g., 0.75 μm in Fig. 1.1), and the water-absorbing wavelengths are typically selected from near-infrared bands, such as 1.6 μm, 2.1 μm, and 3.6 μm. Among these three bands, water absorption is weakest at 1.6 μm and strongest at 3.6 μm. As shown in Fig. 1.1, under the assumption of a plane-parallel atmosphere, the reflectance at 0.75 μm increases monotonically with increasing cloud optical depth (τ) and only weakly depends on cloud effective radius (r_e). In contrast, the reflectance at 2.16 μm is primarily determined by r_e and less sensitive to τ. By computing reflectance for a range of τ and r_e at a given sun-viewing geometry and surface albedo, one can generate lookup tables (e.g., Fig. 1.1), which can then be compared against observed reflectance to retrieve τ and r_e simultaneously. Note that signals for optically thin clouds are relatively weak and can introduce significant uncertainty in retrievals. Retrievals for very small cloud droplets (e.g., r_e of 2 μm) also be challenging can due to ambiguous solutions.

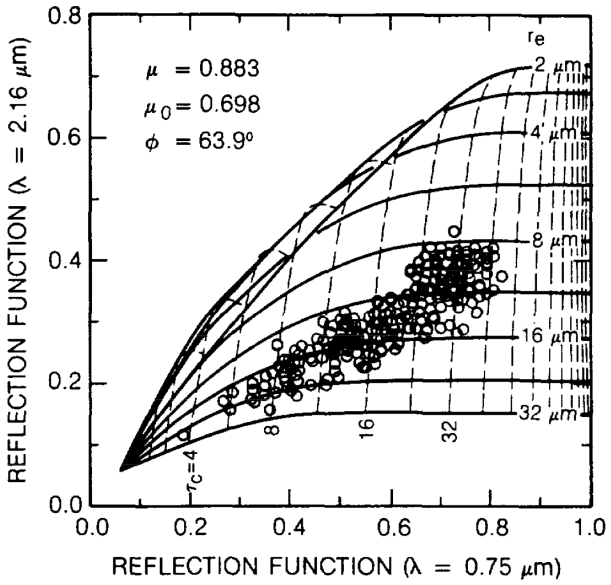

Figure 1.1. Theoretical relationships between the reflectance function at 0.75 μm and 2.16 μm for various optical depths and effective radii at solar zenith angle of 45.7°, viewing zenith angle of 28.0° and viewing azimuth angle of 63.9°. Taken from Nakajima and King (1990)

1.3. Cloud retrievals errors introduced by the plane-parallel assumption and 1D radiative transfer (RT)

Reflectances in the lookup table used for the retrieval method above are computed using one-dimensional (1D) radiative transfer with a vertically homogeneous, plane-parallel homogenous layer. These simplified cloud morphology assumptions introduce errors in retrieved cloud properties.

One source of error comes from ignoring sub-pixel cloud variability (also known as unresolved variability), which leads to an underestimation of retrieved r_e and τ (Marshak et al., 2006). To explain this systematic error, consider a cloud pixel that contains two sub-pixels of reflectances R_1 and R_2 and effective radii r_{e1} and r_{e2}, respectively (see Fig. 1.2(a)). The "true" effective radius is the average of r_{e1} and r_{e2}, and the instrument will observe the average pixel reflectance, $(R_1+ R_2)/2$. Due to the convex, monotonically decreasing shape of reflectance as a

function of effective radius for a water-absorbing wavelength, the observed reflectance corresponds to the effective radius (r_e^*), which is smaller than the true effective radius, (r_{e1}+ r_{e2})/2. Similarly, the impact of ignoring sub-grid cloud variability on cloud optical depth can be conceptualized using a pixel with two sub-pixels with different optical depths, τ_1 and τ_2, as shown in Fig. 1.2(b). Because the relationship between reflectance and optical depth is concave, the observed reflectance corresponding to τ^*, which is smaller than the true average optical depth $(\tau_1 + \tau_2)/2$.

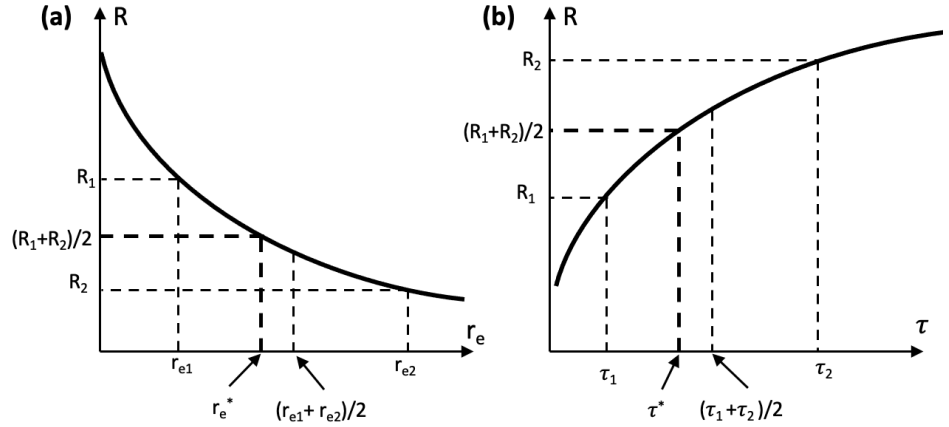

Figure 1.2. Illustration of reflectance (R) versus (a) cloud effective radius (r_e) and (b) cloud optical depth (τ). Dashed lines are used to represent the correspondence of R on these cloud properties. Adapted from Marshak et al. (2006).

The example above introduces sub-grid variability using two sub-pixels with different cloud properties, leading to an overcast pixel. However, a pixel can be filled by partly clear sky and partly by clouds. For such a partially cloudy (PCL) pixel, the retrieval error depends on cloud fraction and cloud properties in the scene. Werner et al. (2018) used measurements from the Advanced Spaceborne Thermal Emission and Reflection Radiometer (ASTER) at 30 m to quantify errors in cloud retrievals. Similar to the overcast pixels, they found an underestimation in cloud optical depth in PCL pixels. This is because dark oceans in clear-sky portions lower the average TOA reflectance of the pixel, leading to a smaller optical depth and underestimation. As expected,

when cloud fraction decreases, there is a greater reduction in TOA reflectance, which leads to a larger underestimation in retrieved cloud optical depth. In contrast, the reduction in TOA reflectance mainly leads to an overestimation in retrieved cloud effective radius.

Errors due to ignoring sub-grid cloud variability can be reduced by enhancing the spatial resolution of pixels. Using cloud retrievals at a spatial resolution of 30 m from ASTER measurements as a reference, Werner et al. (2018) characterized retrieval errors at 1 km and 240 m due to sub-grid cloud variability, as shown in Table 1.1. Enhancing spatial resolution to 240 m greatly helped reduce the 50th percentile of retrieval errors to within 10%. Note that all the comparisons listed in Table 1.1 are based on 1D cloud retrievals, and errors due to 3D radiative effects are not included yet.

Table 1.1. Retrieval errors defined as the difference between the pixel-level retrievals and the 30-m sub- pixel cloud properties (treated as the truth, though they are 1D retrievals). The 1st, 50th and 99th percentiles of the error distributions are listed, based on Werner et al. (2018).

Variable / Resolution	1st	50th	99th
Cloud optical depth τ / 1 km	−62.98 %	−22.30 %	−7.68 %
Cloud optical depth τ / 240 m	−19.74 %	−5.99 %	3.73 %
Cloud effective radius r_e (μm) / 1 km	−34.60 %	3.54 %	38.36 %
Cloud effective radius r_e (μm) / 240 m	−14.24 %	−2.53 %	5.51 %
Liquid water path (g m^{-2}) / 1 km	−72.00 %	18.67 %	1.40 %
Liquid water path (g m^{-2}) / 240 m	−26.21 %	−1.72 %	10.70 %
N_d (cm^{-3}) / 1 km	−68.37 %	−18.41 %	104.15 %
N_d (cm^{-3}) / 240 m	−25.00 %	0.77 %	31.81 %

Another source of errors comes from ignoring 3D cloud effects. 1D RT calculations used in the construction of lookup tables do not allow horizontal transport and in turn ignore cloud inhomogeneity at scales larger than the pixel size. To understand the impact of ignoring 3D RT effects on cloud retrievals, Marshak et al. (2006) discussed the impact of illumination and shadowing and provided theoretical explanations of the overall impacts. Let us suppose that τ and

r_e are independently retrieved, and that the scene has the same numbers of illuminated and shadowed pixels with the same magnitude but a different sign of reflectance changes. In their definition, the illumination and shadowing are based on the reflectance difference between 1D and 3D RT, rather than the relative location of pixels to the sun and viewing geometry. If the reflectance in 3D RT (i.e., the reflectance that the instrument will measure) is *larger* than that in 1D RT, the pixel is illuminated. If the reflectance in 3D RT is *smaller* than that in 1D RT, the pixel is shadowed. From Fig. 1.2, we see that the smaller reflectance observed at shadowed pixels will lead to a larger retrieved r_e than its 1D counterpart. In contrast, the enhanced reflectance observed at the illuminated pixel leads to a smaller retrieved r_e than its 1D counterpart. If the illuminated and shadowed pixels have the same magnitude of changes in reflectance, then the increase in retrieved r_e from shadowed pixels is larger than the decrease in retrieved r_e from illuminated pixels, because reflectance decreases faster with increasing r_e at small r_e and the curve in Fig. 1.2(a) becomes flat at large r_e (i.e., a small change in reflectance leads to a large change in r_e). If the number of illuminated and shadowed pixels are the same, then the integrated impact from illumination and shadowing together is an overestimate in retrieved r_e. A similar argument can be developed using Fig. 1.2(b) for τ, leading to a finding of overestimated τ if 3D effects are ignored during the retrieval process.

These theoretical explanations are further supported by the results using synthetic datasets generated from LES (Marshak et al., 2006; Okamura et al., 2017). In general, scenes with broken cumulus clouds tend to have a larger overestimation in retrieved τ and r_e, compared to stratocumulus scenes (Marshak et al., 2006). For closed cells and open cells found in the stratocumulus regime, Table 1.2 shows the error statistics between 1D and 3D retrievals for solar zenith angles of 20° and 60°. Surprisingly, the retrieval errors between closed cells and open cells

are comparable, highlighting the importance of incorporating 3D effects in retrieval methods. Overall, incorporating 3D cloud effects can significantly reduce retrieval errors in both τ and r_e, especially for cases with large solar zenith angles.

Note that the 3D retrieval method in Table 1.2 is machine-learning based. To incorporate 3D radiative effects in cloud retrievals, Okamura et al. (2017) used LES output and 3D RT to generate a training dataset with ~2M samples containing pairs of reflectance at multiple MODIS wavelengths. A Convolution Neural Network was built using this training dataset and provided predictions of column τ and r_e.

Table 1.2. The relative root-mean-squared error of retrieved cloud τ and r_e reported in Okamura et al. (2017), using large-eddy simulations to generate the synthetic data. The retrievals were made from the synthetic reflectance at wavelengths of 0.86, 1.64, 2.13, and 3.75 μm at 280 m resolution. The 3D method uses convolution neural network for predicting column cloud τ and r_e, based on ~2 million training data.

Retrieval method	Cloud optical depth		Cloud effective radius	
	Open cell	Closed cell	Open cell	Closed cell
1D, SZA=20°	30.7 %	16.0 %	38.3 %	51.2 %
3D, SZA=20°	21.6 %	23.4 %	5.5 %	6.7 %
1D, SZA=60°	74.8 %	50.9 %	51.1 %	55.2 %
3D, SZA=60°	26.6 %	18.7 %	6.5 %	7.3 %

1.4. Review of existing efforts for 3D cloud retrievals

In addition to the known biases in retrieved τ and r_e, another limitation of existing cloud products is the lack of information on 3D cloud fields. Only very few methods have attempted to retrieve 3D cloud fields. Barker et al. (2011) first proposed to reconstruct 3D cloud fields by combining CPR and MODIS measurements. CPR measurements are used to provide critical information on vertical cloud profiles, but they are only available along the nadir track of the satellite path. To reconstruct a 3D cloud field, information on cloud vertical structure from CPR

at nadir pixels needs to be propagated to off-nadir pixels. As shown in Fig. 1.3, this propagation was done using a "donor-recipient" approach that is started by matching MODIS radiance between nadir pixels and off-nadir pixels under similar conditions with surface type and the sun-viewing geometry. In their studies, most donors and recipients can be found within 30 km from each other. When the match is found, vertical profiles of liquid water content and ice water content derived from CPR measurements from the nadir pixel (called "donor") are assigned to the off-nadir pixel (called the "recipient"). The water content profiles at recipient pixels are further normalized by the scaled τ retrieved from MODIS at recipient pixels. Since the MODIS retrievals used in Barker et al. (2011) are based on 1D RT, the resulting reconstruction does not incorporate information on cloud inhomogeneity and 3D radiative effects.

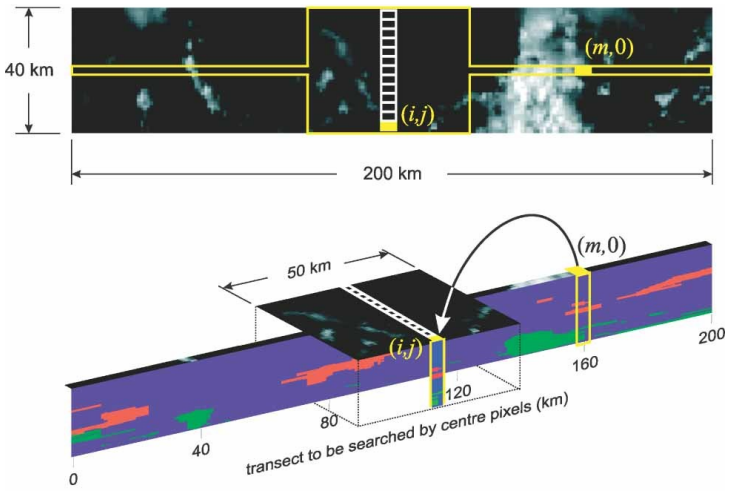

Figure 1.3. Schematic of the "donor–recipient" matching processes to assign vertical profile information from nadir pixels to off-nadir pixels. The top panel shows a 200-km wide and 40-km long swath of MODIS imagery with the CloudSat and CALIPSO track in the middle where the pixel (m, 0) is located. The bottom panel shows the "curtain" of vertical cloud observations from CloudSat and CALIPSO, where the red and green indicate different cloud features. An off-track pixel, labeled (i, j), is found to have a matched MODIS reflectance value with a nadir pixel, labeled (m, 0). The cloud profile at (m, 0) is then donated to (i, j), and we call (m, 0) and (i, j) 'donor' and 'recipient', respectively. Taken from Barker et al. (2011).

Leinonen et al. (2019) argued that the match-up process based on radiance in Barker et al. (2011) could create somewhat unrealistic 3D cloud fields. To alleviate this issue, they used a conditional generative adversarial network (CGAN) to predict the vertical profile of radar reflectivity for each MODIS pixel. The CGAN was trained using collocated MODIS-derived cloud properties and CloudSat radar profiles in scenes that are 70 km horizontally along-track, and 15 km in height. Since it was trained scene-by-scene, the CGAN provides a "curtain" plot of radar reflectivity, given a set of MODIS-retrieved cloud top pressure, cloud optical depth, effective radius, and cloud water path along the track. In general, the performance of the CGAN in radar profile predictions is promising, and one can further apply the scaling method described in Barker et al. (2011) to scale radar-retrieved liquid and ice water content profiles by MODIS-retrieved optical depth. However, since the CGAN basically uses the combination of 1D cloud optical and microphysical retrievals to "define" radar reflectivity, it is unclear what the associated cloud retrieval errors are in each scene, and how those errors propagate into the network and affect its prediction. Additionally, since this framework is tied with 1D cloud retrieval as part of the training, the goal of accounting for 3D radiative effects in the retrieval cannot be achieved by this CGAN approach.

Incorporating 3D radiative effects in the retrieval process requires some means to perform 3D RT sufficiently fast for the updated solution of cloud fields. However, the existing 3D RT methods remain too slow to be incorporated. Most fast schemes have been developed for flux calculations due to the need in weather and climate models. For example, one of the promising methods is the ten-stream scheme (Jakub & Mayer, 2015). This method discretizes direct radiation into four directions and diffuse radiation into six directions. Although they have focused on calculations of flux and heating rate, in principle, the ten-stream scheme can be used to compute

reflectance at the top of the atmosphere, but the performance is unknown. There is an emulator for RT calculations in the microwave spectral region (Liang et al., 2022), but this only works for clear-sky and does not handle scattering radiation, as needed in applications in visible and near-infrared spectral regions. The lack of a fast 3D RT scheme for remote sensing applications has prevented us from moving forward to 3D cloud retrievals.

1.5. Outline of Thesis

As explained above, existing retrieval methods cannot simultaneously retrieve 3D cloud fields and incorporate 3D radiative effects. Many retrieval methods for clouds, however, have moved on from traditional lookup table approaches to more rigorous optimization frameworks such as the variational method (Mason et al., 2022) and iterative Ensemble Kalman filter (Fielding et al., 2014, 2015), although in principle, these methods can still use lookup tables in the forward model calculations. For these advanced retrieval methods, 3D radiative effects can be incorporated if 3D RT is used as part of the forward model. However, the iterative nature of the retrieval method requires 3D RT to be computed fast. This thesis aims to develop such a fast 3D RT scheme for those advanced retrieval methods and remote sensing applications in general. Specifically, this thesis focuses on tdeveloping a fast RT scheme for reflectance calculations at visible and near-infrared wavelengths using machine learning techniques. In Chapter 2, the performance and development of the 3D reflectance emulator will be introduced and detailed. The retrieval method under development uses A-Train satellite observations and is planned to be evaluated against in-situ data collected from the Variability of the American Monsoon Systems (VAMOS) Ocean-Cloud-Atmosphere-Land Study Regional Experiment (VOCALS-REx) field campaign. In Chapter 3, the observational datasets, including MODIS, CloudSat, CALIPSO, and VOCALS-REx, will be described. In Chapter 4, we evaluate the new 3D cloud microphysical property retrievals and

compare them against 1D methods using a synthetic dataset. Finally, in Chapter 5, we will discuss how these elements will be used in the retrieval method in the future.

CHAPTER 2: 3D EMULATOR FOR SHORTWAVE REFLECTANCE AT TOA

This chapter details the development of fast 3D RT emulators for computing reflectance at the top of the atmosphere (TOA) for the use in advanced retrieval methods. The emulator is designed to match MODIS wavelengths of 645 nm, 857 nm, and 2113 nm. Since the finest spatial resolution corresponding to these wavelengths is 250 m, the emulator is built to provide reflectance with this spatial resolution.

2.1. Emulator setup and training

The 3D emulators use a Convolution Neural Network (CNN), as shown in Fig. 2.1. The emulators will be trained by a dataset that contains a pair of input fields and output reflectance. The input includes 3D fields of liquid water content (LWC) and r_e, and 1D profiles of aerosol and gas optical properties. The output is reflectance at TOA for a 1.25 km x 1.25 km domain. The construction of the training dataset is detailed next.

We first built a dataset of 3D cloud fields. Since 3D radiative effects are largest for highly heterogenous clouds such as cumulus regimes (Hogan & Shonk, 2013; Pincus et al., 2005), our training dataset is based on shallow cumulus simulations produced by the Large Eddy Simulation (LES) Atmospheric Radiation Measurement (ARM) Symbolic Simulation and Observation (LASSO) Activity with a focus on the Southern Great Plains (SGP) site in Oklahoma (Gustafson et al., 2020). Example cloud fields are shown in Fig. 2.2, and a total of 235 cloud fields were selected with cloud fractions ranging between 0.2 and 0.8. The LASSO simulations have a horizontal resolution of 100 m and a vertical resolution of 30 m. Since the emulator is planned to be applied to A-Train observations, the horizontal and vertical resolutions were set as 250 m and 60 m, respectively, and will be explained in more detail in Chapter 3. Hence, for the vertical, the

30-m liquid water content was averaged to a resolution of 60 m. For the horizontal, the 100 m liquid water content was first re-gridded to 50 m, then averaged to 250 m resolution. Additionally, since these simulations only provide liquid water content without droplet size information for each grid point, we have assumed a fixed N_c of 50 cm^{-3} and computed the corresponding r_e by assuming a lognormal cloud DSD with a geometric standard deviation (σ) of 0.3 and using the following relationship:

$$LWC = \frac{4\pi\rho_w}{3} N_c r_{e,c}^3 \exp(-3\sigma^2). \tag{2.1}$$

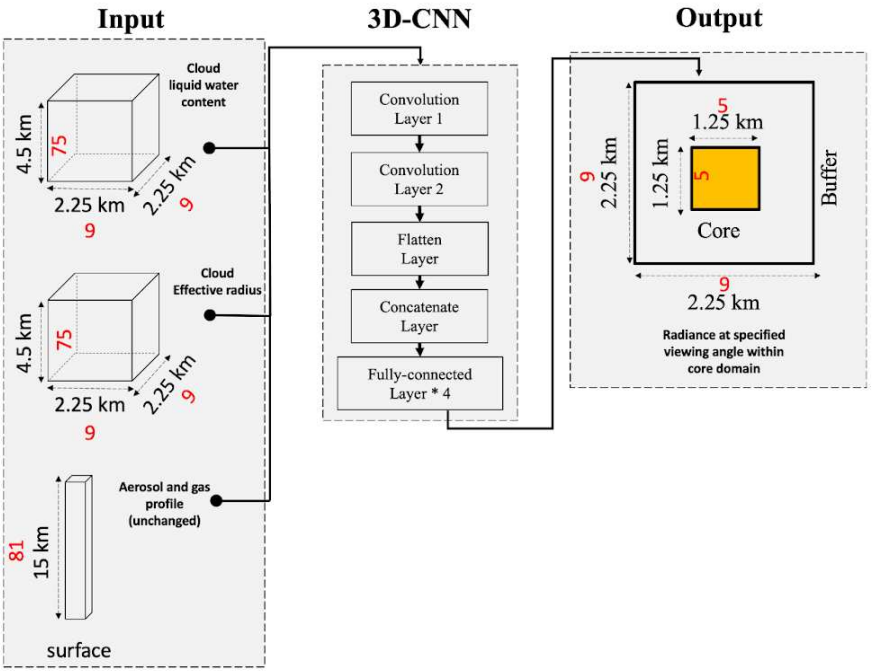

Figure 2.1. A flowchart showing the configuration of the 3D radiative transfer emulator. The dimensions of the domains are labeled in black, and the number of grid points are labeled in red. The core domain for the reflectance output is filled in yellow. An emulator is trained at one specific wavelength and one set of viewing and solar geometry. Modified from Yang (2022).

The cloud fields have a variety of cloud sizes and cloud fractions, such as smaller, scattered cumulus fields with a thickness of less than 300 m (Fig. 2.2 (a)) and larger, geometrically thicker cumulus clouds (Fig. 2.2 (b)). Snapshot statistics of the cloud fields are shown in Fig. 2.3. The 25th and 75th percentiles of cloud geometric thickness are 0.18 km and 0.8 km, respectively (see Fig. 2.3 (b)), while the cloud base and cloud top heights have a much larger range across the cloud fields (see Fig. 2.3 (a)).

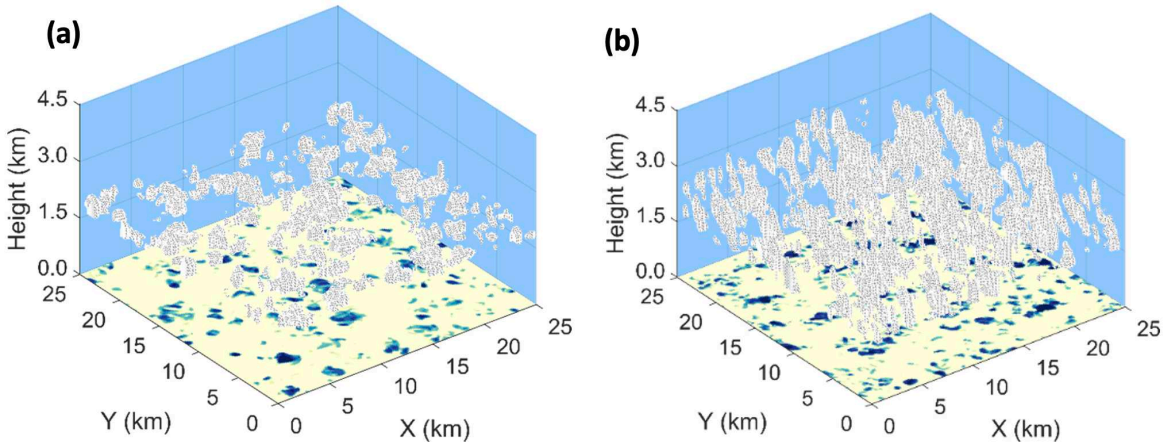

Figure 2.2. Example LASSO cloud fields at 100 m x 100 m x 30 m resolution with x-, y- and z-direction, respectively. (a) shows a field of scattered shallow cumulus and (b) a field of large cumulus. Liquid water path is shown on the x-y plane, and the clouds are represented as a grey iso-surface. Taken from Yang (2022).

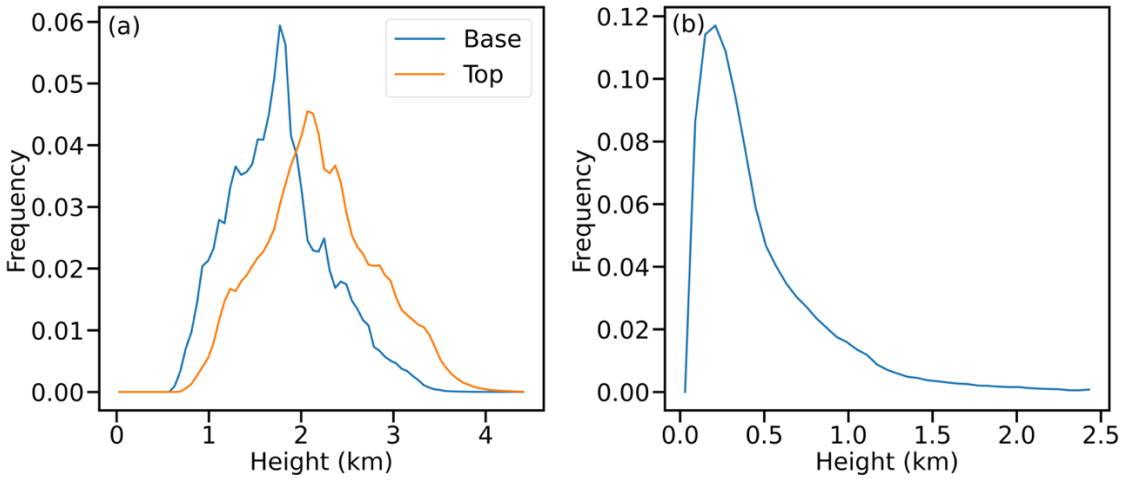

Figure 2.3. LASSO cloud field statistics for each cloudy column within all 235 scenes. Calculated for 250 m x 250 m x 60 m interpolated scenes. Histograms of (a) cloud base height and cloud top height and (b) cloud geometric thickness.

In addition to cloud fields, information on aerosols is also required for computing reflectance at TOA. The aerosol properties (e.g., location, aerosol type, and particle size) used in the training and testing datasets were based on both the in-situ aircraft data from one of the VOCALS-REx flights and MODIS retrievals on 11 November 2008. First, the aerosol size distributions were obtained by the Passive Cavity Aerosol Spectrometer Probe (PCASP) which measures particles in a size range between 0.1 and 20 μm (Zheng et al., 2011; Cai et al., 2013). Using these measurements, the aerosol effective radius (r_a) was calculated by (Jia et al., 2019):

$$r_a = \frac{\sum n_i r_i^3}{\sum n_i r_i^2}, \tag{2.2}$$

where n_i and r_i are the aerosol number concentration and center radius of the *i*th bin, respectively. This calculation was applied to the period when the aircraft made a complete ascent and descent during 18:55–19:30 UTC. The histogram of these aerosol effective radii and a scatterplot of aerosol number concentration versus altitude are shown in Fig. 2.4. From Fig. 2.4 (a), we found that aerosols have a bimodal size, with a fine mode peaked at 0.2 μm and a coarse aerosol mode peaked at 1.3 μm. From Fig. 2.4 (b), we found that aerosol number concentration is relatively constant (200–400 cm^{-3}) up to ~1 km height and then decreases dramatically and becomes negligible above 1 km. Based on this analysis, we place an aerosol layer from the surface to 1 km in the later RT calculations. Note that regions with a greater density of pixels merely indicate that the aircraft made more measurements at that altitude.

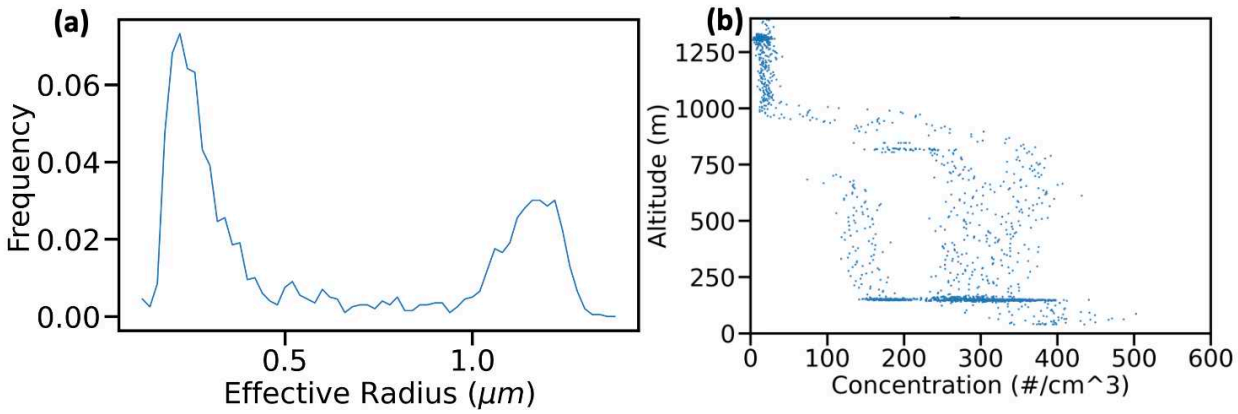

Figure 2.4. (a) Histogram of aerosol effective radius and (b) plot of altitude vs aerosol number concentration, derived from PCASP measurements between 18:55 UTC and 19:30 UTC during VOCALS-REx Research Flight #12.

Aircraft observations in Fig. 2.4 are generally consistent with MODIS retrievals, as shown in Fig. 2.5. Details of aerosol types used in MODIS can be found in Table 2.1. For the fine mode, MODIS retrievals are domined by water soluble aerosols (Type 1), but the r_a observed in the VOCALS-REx campaign is about 0.2 μm, which is more consistent with MODIS Type 3 aerosol (water soluble with humidity). Since we focus on cloudy regions, aerosol type of water soluble with humidity appears more appropriate and will be used in our RT calculations. For the coarse mode, r_a observed in the VOCALS-REx campaign is consistent with MODIS type 5 aerosol, and thus the properties of wet sea salt will be used. The fine mode fraction is set as 0.7, based on MODIS retrievals.

Once the aerosol types were determined, along with the information on refractive index and size distribution in Table 2.1, the volume extinction coefficient of the aerosols were calculated using the Mie Theory. Since the retrieval from the closest NASA Aerosol Robotic Network (AERONET) site in Arica, Chile was about 0.1 on 11 November 2008, and generally consistent with MODIS retrievals, we partitioned the total aerosol optical depth of 0.1 to fine mode and coarse mode. We applied a fine mode aerosol number concentration of 1.72×10^{-5} cm^{-3} and a coarse

mode aerosol number concentration of 3.05×10^{-5} cm^{-3} throughout the aerosol layer between 0–1 km in RT calculations. The aerosol mass density, ρ, was referenced using the Optical Properties of Aerosols and Clouds (OPAC) database Gestion et Etude des Informations Spectroscopiques Atmospheriques (GEISA)-03 product. The fine and coarse mode densities were given 1.8 g m^{-3} and 2.2 g m^{-3}, respectively.

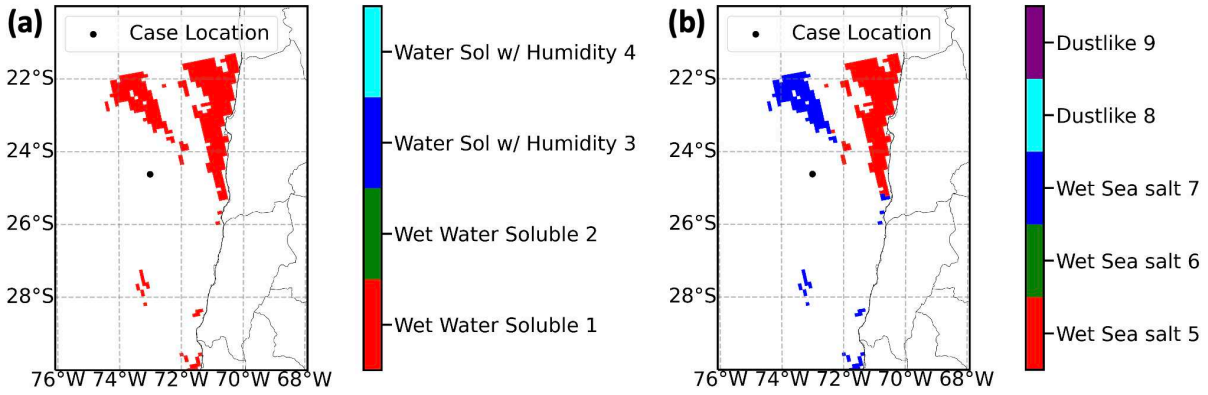

Figure 2.5. Types of aerosol (a) fine mode and (b) coarse mode retrieved from MODIS observations on 11 November 2008, available in the operational MYD04 aerosol product. The vertical profile location identified in section 2.1 is marked with a black dot.

Table 2.1. Aerosol properties for fine modes (F1-F4) and coarse modes (C5-C7) used in MODIS lookup table for the ocean algorithm. For each aerosol mode, included are aerosol refractive indices by wavelength (λ), median aerosol radius (r_g), distribution standard deviation (σ), and aerosol effective radius (r_{eff}). This table is taken from the MODIS MYD04 ATDB (Table 2A of Remer et al., 2009).

F	λ=0.47-->0.86μm	λ =1.24μm	λ =1.64μm	λ =2.12μm	r_g	σ	r_{eff}	Comments
1	1.45-0.0035i	1.45-0.0035i	1.43-0.01i	1.40-0.005i	0.07	0.40	0.10	Water Soluble
2	1.45-0.0035i	1.45-0.0035i	1.43-0.01i	1.40-0.005i	0.06	0.60	0.15	Water Soluble
3	1.40-0.0020i	1.40-0.0020i	1.39-0.005i	1.36-0.003i	0.08	0.60	0.20	Water Soluble with humidity
4	1.40-0.0020i	1.40-0.0020i	1.39-0.005i	1.36-0.003i	0.10	0.60	0.25	Water Soluble with humidity

C	λ =0.47-->0.86μm	λ =1.24μm	λ =1.64μm	λ =2.12μm	r_g	σ	r_{eff}	Comments
5	1.35-0.001i	1.35-0.001i	1.35-0.001i	1.35-0.001i	0.40	0.60	0.98	Wet sea salt type
6	1.35-0.001i	1.35-0.001i	1.35-0.001i	1.35-0.001i	0.60	0.60	1.48	Wet sea salt type
7	1.35-0.001i	1.35-0.001i	1.35-0.001i	1.35-0.001i	0.80	0.60	1.98	Wet sea salt type

We also included gas absorptions due to water vapor, ozone, and other gasses, including CO_2, CO, N_2O, NO_2, NO, CH_4, O_2, and SO_2, as the absorptions of these gases are considered in the operational MODIS aerosol algorithm (see Table 2.2). To properly account for these gas absorptions and match the total optical depth listed in Table 2.2, we used the vertical profile in the tropics from the database in the Santa Barbara Discrete Ordinates Radiative Transfer Program for a Multi-Layered Plane-Parallel Medium (DISORT) Atmospheric Radiative Transfer Model (SBDART), and then scaled these profiles with the optical depth listed in Table 2.2. Lastly, for calculations of ocean reflectance, we have used a wind speed of 7 m s^{-1} based on the Medium-Range Weather Forecast (ECMWF) Reanalysis v5 (ERA5; Hersbach et al., 2020) and a chlorophyll pigmentation level of 0.13 mg m^{-3} based on the surface chlorophyll mass concentration retrieved in the MODIS ocean color product (L2/OC).

Table 2.2. Gas absorption coefficients used within the MODIS algorithms. K coefficients are gas absorption coefficients to adjust gas profiles and were not used in our calculations. Taken from (Patadia et al. (2018)).

MODIS band	Wavelength (μm)	Rayleigh optical depth	O_3 optical depth[a]	H_2O optical depth[a]	Dry-gas[b] optical depth[a]	O_3_K0	O_3_K1	H_2O_K0	H_2O_K1	H_2O_K2
B3	0.4659	1.92E-01	2.90E-03	8.00E-05	1.25E-03	−1.14E-04	8.69E-06	−9.58E+00	1.23E+00	−1.16E-01
B4	0.5537	9.44E-02	3.26E-02	5.00E-04	9.50E-04	5.18E-06	9.50E-05	−7.91E+00	1.00E+00	−1.29E-02
B1	0.6456	5.08E-02	2.52E-02	5.11E-03	3.91E-03	1.16E-04	7.32E-05	−5.60E+00	9.40E-01	−1.78E-02
B2	0.8564	1.62E-02	8.10E-04	8.61E-03	2.00E-05	2.80E-07	2.36E-06	−5.07E+00	8.77E-01	−2.40E-02
B5	1.2417	3.61E-03	0.00E+00	5.23E-03	1.69E-02	1.19E-07	1.55E-25	−5.65E+00	9.81E-01	−2.38E-02
B6	1.6285	1.22E-03	0.00E+00	1.62E-03	9.98E-03	1.19E-07	5.17E-26	−6.80E+00	1.03E+00	−4.29E-03
B7	2.1134	4.30E-04	2.00E-05	2.53E-02	1.63E-02	6.29E-07	7.03E-08	−3.98E+00	8.86E-01	−2.56E-02

[a] For each MODIS band, this nadir-looking (viewing zenith angle = 0) optical depth for the gas is computed from the US 1976 Standard Atmosphere in LBLRTM.
[b] Dry gas includes CO_2, CO, N_2O, NO_2, NO, CH_4, O_2, SO_2.

All the information on the clouds, aerosols, gases, and surface will be used as input for the 3D version of the Spherical Harmonic Discrete Ordinary Method (SHDOM; Evans, 1998) to compute the reflectance at TOA at 645 nm, 857 nm, and 2113 nm. We have built separate emulators for each wavelength and for four sets of sun-viewing geometry listed in Table 2.3. These

sets are chosen to cover different solar angles and to include the geometry that matches the VOCAL-REx case.

Table 2.3. Sun-viewing geometries used in emulators. Azimuth angles are defined as the angle from the north. The 4th set is based on the geometry in the VOCALS-REx case.

Index	Solar zenith angle (º)	Solar azimuth angle (º)	Viewing zenith angle (º)	Viewing azimuth angle (º)
1	20	270	0	0
2	60	270	0	0
3	33	264	0	281
4	33	264	18	281

As shown in Table 2.3, the sensor for one of the emulators is away from the local zenith, which leads to a shift in the spatial distributions between the reflectance and cloud fields, so-called the "parallax effect". Figure. 2.6 shows the basic concept of the parallax shift, which needs to be corrected before training the CNNs. Following Kostka et al. (2014), the parallax shifts in the x- and y- directions, respectively denoted as Δx and Δy, can be calculated by:

$$\Delta x = \Delta z \ \tan\theta \cos\varphi, \tag{2.3}$$

$$\Delta y = \Delta z \ \tan\theta \sin\varphi, \tag{2.4}$$

where Δz is the difference between the cloud top height and the output plane, θ and φ are viewing zenith and azimuth angles, respectively.

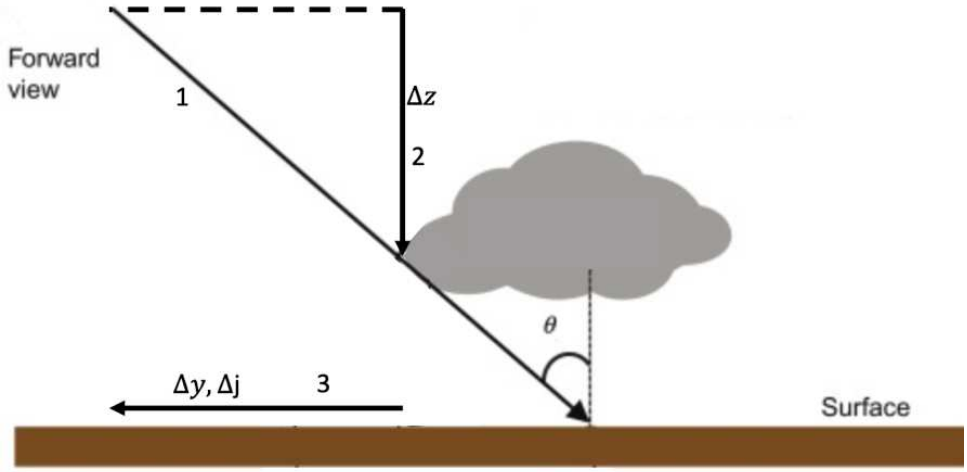

Figure 2.6. Diagram illustrating the parallax shift magnitude Δj on a portion of a cloud. Arrow 1 represents the satellite view. The viewing zenith angle (θ) and distance from the output plane to the cloud top height of a pixel (Δz, arrow 2) determine the magnitude of the shift (Δy, arrow 3). The shaded area represents pixels with clouds and the arrow 3 represents the magnitude of the shift. This distance is converted into the number of pixels (Δj) shifted.

In practice, the shifts Δx and Δy need to be converted to the number of grids for corrections. To correct parallax effects as accurately as possible, we first re-grid cloud fields from the horizontal resolution of 250 m to 50 m. This re-gridded field is used to calculate reflectance at TOA, shifted for parallax corrections, and then gridded back to 250 m. We have found that this process is necessary and greatly improves the performance of the emulators.

To train the emulator, the 235 cloud fields were split into 80% testing scenes, 10% training scenes, and 10% validation scenes. We also ensured that scenes from the same day would be sorted into only one of the three categories. This is because cloud scenes from the same day may have similar cloud structures, so including scenes from the same day within both testing and training would bias the evaluation of the emulator performance. Each cloud field was 25 km x 25 km and was given a padding of 25 km in the x-direction and 5 km in the y-direction to allow for parallax shifts. One such field, the output from SHDOM, is shown in Fig. 2.7.

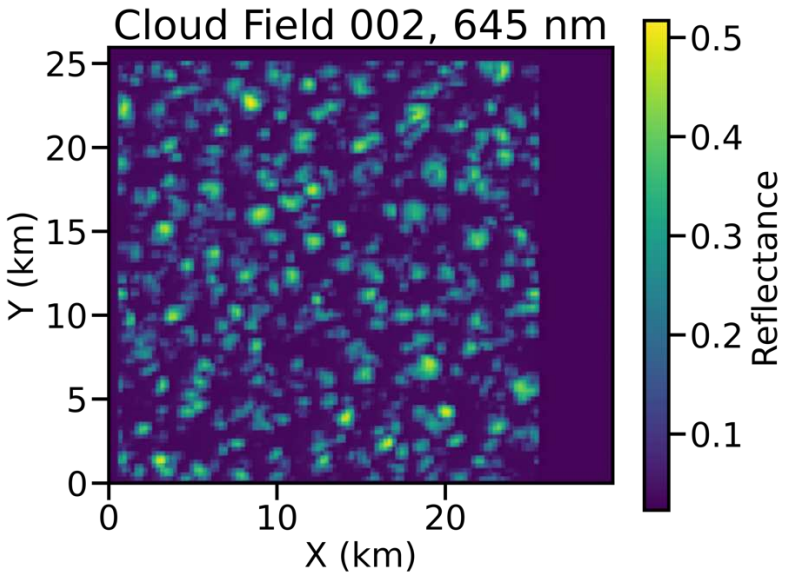

Figure 2.7. Example output scene of reflectance at 645 nm, simulated from SHDOM with a viewing zenith angle of 18° and a viewing azimuth angle of 281° from north. Due to parallax, the scene has shifted in the negative x- and y- directions, which is why the padding is added.

Each cloud field is further used to sample 8281 scenes of 2.25 km x 2.25 km, each shifted 1 by 1 pixel in the x-direction and then y-direction. All scenes from each cloud field are placed into either the training or testing dataset to avoid data leakage. These are the scenes which the emulators are trained on, with a total of ~1.5 million scenes in the training dataset, and ~200,000 scenes each in the testing and validation datasets. The input for emulators is the 3D LWC and r_e fields in these scenes up to 4.5 km in the vertical. The output is reflectance at a smaller domain with a size of 1.25 km x 1.25 km. We will call this smaller domain the "core domain" and the region that is outside the smaller domain but within the scene the "buffer zone" hereafter. The choice of the scene size is based on Okamura et al. (2017), which showed that this size is sufficiently large for incorporating the radiative effects of cloudy pixels in the buffer zone on the reflectance in the core domain.

As the parallax corrections are most accurate when applied to the cloud top height of each scene, separate calculations were made for each one. This scene-selection and parallax-correction process is shown in Fig. 2.8. First, a 2.25 km cloud scene is selected, and we define a cloudy grid

if the associated LWC is equal to or greater than 0.01 g m^{-3}. Based on the core domain within that scene, the mean cloud top height is selected. If no clouds are within the core domain, then clouds in the buffer will be included. The parallax correction calculation is applied using the cloud top height to find the corresponding reflectance field, shown in Fig. 2.8 (b). This also shows some of the limitations of this parallax shift technique, as the reflectance of each cloud pixel "bleeds" into other pixels to some extent, which can never fully be removed. This means the 250 m averaged pixels have some reflectance from nearby pixels incorporated into them. This limits the accuracy of the emulator. Finally, reflectance values at 50-m resolution are averaged into the 250-m resolution, as shown in Fig. 2.8 (c). Note that the scene in Fig. 2.8 is cleaner others, because the associated cloud top heights are relatively uniform. With more variations in the cloud top heights, individual pixels are shifted by different amounts, increasing the degree to which pixels overlap in the reflectance field.

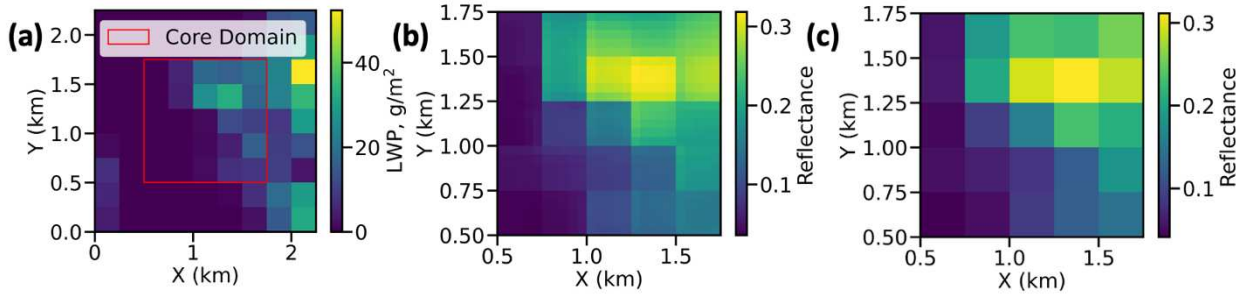

Figure 2.8. The process of correcting for parallax, and averaging form 50 m resolution to 250 m resolution. (a) LWP of an example cloud field scene. The buffer domain is 9x9 pixels, and the core is 5x5 pixels. From the core domain, the average cloud top height is calculated, which is used to determine parallax shift. (b) Based on parallax shift, the corresponding radiance field of the core domain is found in SHDOM (50-m resolution). (c) The 50-m radiance field is then averaged for each 250 m x 250 m pixel. This is the radiance field which is used as "truth" to train the emulator.

2.2. Evaluation of Emulator Performance

2.2.1 Evaluation Metrics

We evaluated the performance of our 3D emulators using several metrics. Since typically only reflectances of cloudy pixels will be used to update the retrieved cloud microphysical properties, the evaluation metrics are also only applied to cloudy pixels. The metrics used are:

$$\text{Single Pixel Error } (SPE_i; \%) = \frac{R_{pred,i} - R_{true,i}}{R_{true,i}} \times 100\% \tag{2.5}$$

$$\text{Mean Error } (\mu_E; \%) = \frac{1}{N}\sum_{i=1}^{N} SPE_i \tag{2.6}$$

$$\text{Error Standard Deviation } (\sigma_E;\ \%) = \left[\frac{1}{N}\sum_{i=1}^{N}(SPE_i - \mu)^2\right]^{\frac{1}{2}}; \tag{2.7}$$

$$\text{Mean Absolute Deviation (MAD; \%)} = \frac{1}{N}\sum_{i=1}^{N}|SPE_i - \mu|; \tag{2.8}$$

$$\text{Error Kurtosis } (K_E; \%) = \frac{\mu^4}{\sigma^4}, \tag{2.9}$$

where $R_{pred,i}$ and $R_{true,i}$ represent the predicted and true reflectance, respectvely, *i* represents the *i*th sample, and *N* represents the total number of samples. SPE_i is the relative error of a single pixel.

2.2.2 Results

We first examined how well the emulators perform for the sun-viewing geometry in our VOCALS-REx case (i.e., the 4th set in Table 2.3). As shown in Fig. 2.9, most data points fall on the 1:1 line, but the low reflectance at all three wavelengths appears more challenging for the emulator to predict well. The histograms of the relative errors for cloudy pixels in Fig. 2.10 nicely show that the median errors are close to zero, and ~70% of pixels have errors within 10%. Based

on Table 2.4, the emulator has similar performances at all three wavelengths, but the statistics at 2113 nm are influenced more by the larger relative errors in the range of small reflectances.

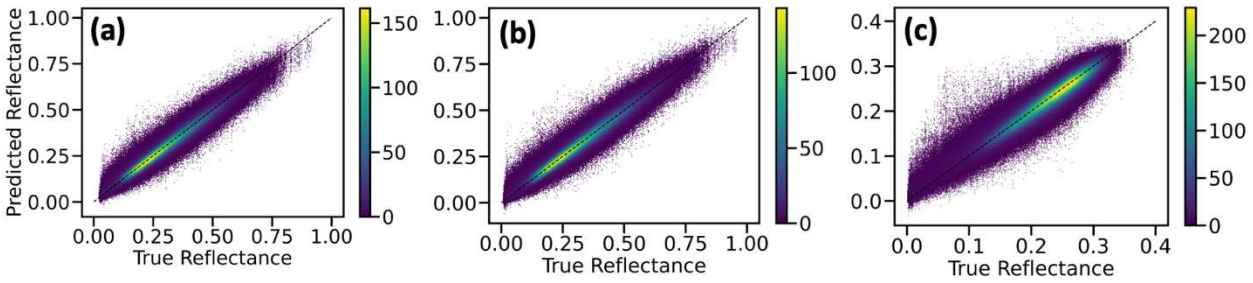

Figure 2.9. Scatter plots of predicted versus truth reflectance for (a) 645 nm, (b) 857 nm, and (c) 2113 nm wavelengths, using the emulator with the sun-viewing geometry of the VOCALS-REx case (i.e., the 4th set in Table 2.3). The black dashed line shows the 1:1 line. The color bar shows the counts of the data points.

Table 2.4. Error statistics used to evaluate emulator performance. The index is used to denote the sun-viewing geometry defined in Table 2.3. λ represents the wavelength (nm), while μ_E, σ_E, MAD, and K_E represent the mean relative errors, the standard deviation of the relative errors, mean absolute deviation, and Kurtosis, respectively; all are in % and calculated by equations (2.5) – (2.9). The percentiles of 15th, 50th, and 85th are also included.

Index	λ	μ_E	σ_E	MAD	K_E	15th	50th	85th
1	645	1.2	6.6	4.6	14	–4.3	1.0	6.4
2	645	2.0	17.1	9.8	27	–9.1	0.2	10.5
3	645	0.9	8.5	5.2	45	–5.3	0.5	6.3
4	645	1.0	14.1	8.2	77	–8.4	–0.3	8.9
4	857	1.6	19.3	8.8	267	–8.2	–0.1	8.9
4	2113	0.6	22.9	8.0	434	–8.0	–1.1	5.9

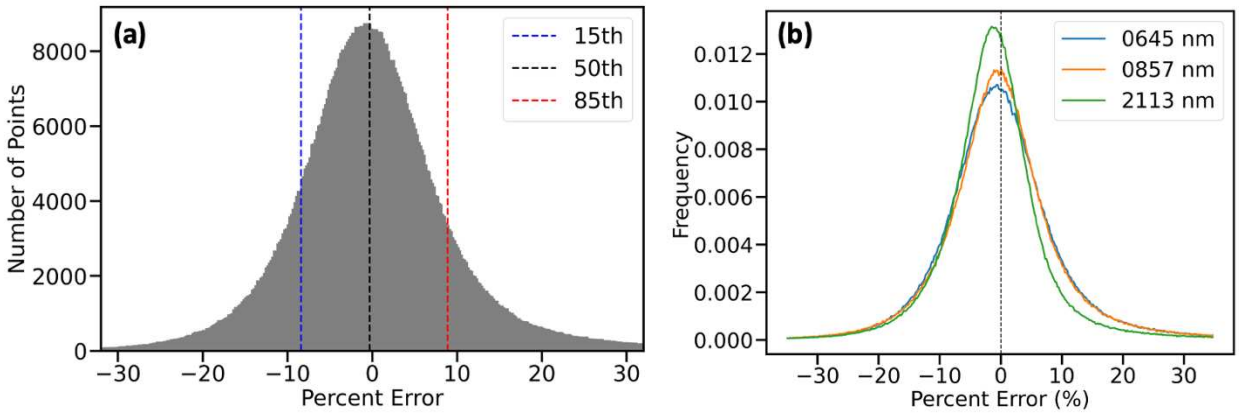

Figure 2.10. Normalized histograms of the relative errors at wavelengths of (a) 645 nm, and (b) all three wavelengths, using the emulators with the sun-viewing geometry in the VOCALS-REx case. In (a), the 15th, 50th, and 85th percentiles are shown, which are at –8.4%, –0.3%, and 8.9%, respectively. Detailed error statistics for all three wavelengths can be found in Table 2.4.

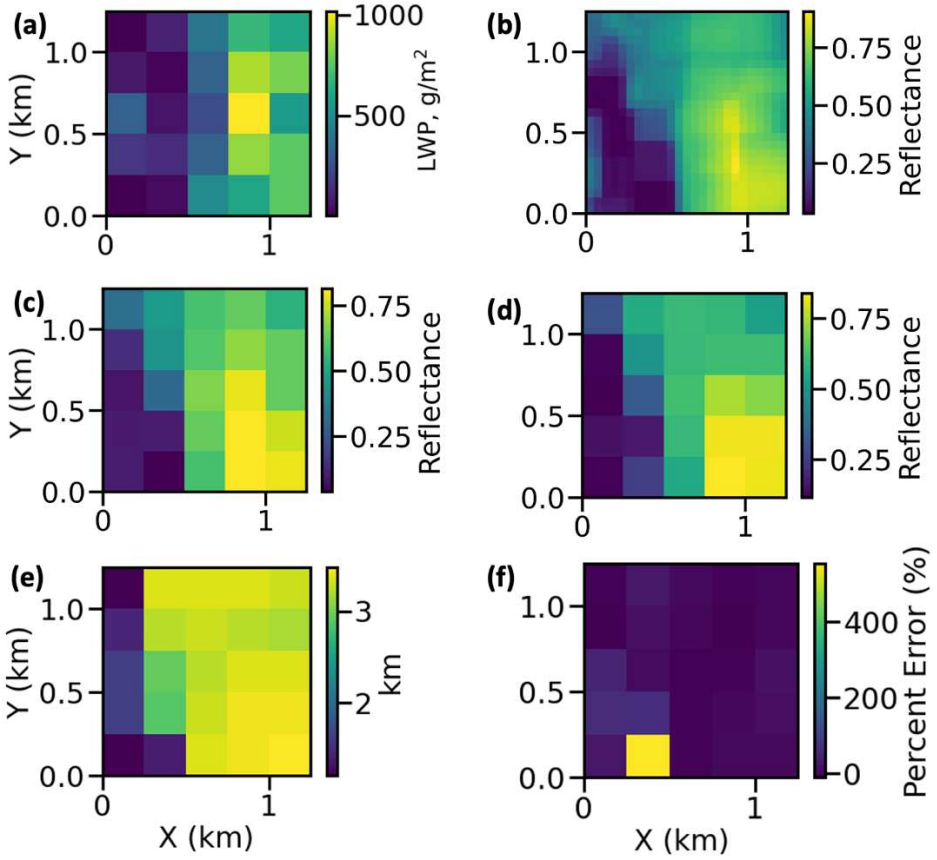

Figure 2.11. An example of cloud scene for illustrating a case with an extremely large errors in reflectance due to parallax effects. Only the core domain is shown in all subfigures. Created from 645 nm reflectance field. The units on the x and y axes are km. (a) Optical depth of the cloud scene. (b) Corresponding 50-m reflectance field. (c) True reflectance field calculated using SHDOM. (d) Emulator-predicted reflectance field. (e) Cloud top height of scene. (f) Percent error for each pixel within the scene.

To highlight the possible source of errors in the range of small reflectance, Fig. 2.11 shows a scene where the challenges of the parallax shifts cause a pixel to have an extremely high relative error of nearly 600%. This is an extreme case where multiple factors converge, but it exemplifies the cause of these large relative errors. Consider Fig. 2.11 (f), where we see the pixel with such a high relative error. From Fig. 2.11 (a), we see that this pixel has a very low τ, especially in comparison to nearby pixels, meaning we would expect this pixel to have a low reflectance. In Fig. 2.11 (b), which shows the 50-m parallax-corrected reflectance prior to averaging, the issue becomes clearer, which is that different pixels have been shifted by different distances because, as shown in Fig. 2.11 (e), the cloud top heights vary significantly across the scene. Most of the cloud top heights are above 3 km, but the pixel with the very large error has a cloud top height closer to 1 km. With our method of parallax correction, each scene can only be shifted by the same amount, and that distance is calculated by the average cloud top height. In this case, that distance is ~3 km, meaning the parallax shift was ~3.9 km, but the pixel at 1 km would have been shifted by 4.5 km, ending up in another scene entirely (and affecting the accuracy of that scene as well). More generally, with the range of cloud top heights in this scene, the reflectances corresponding to each pixel are shifted by various distances, meaning many pixels averaged to 250m resolution, shown in Fig. 2.11 (c), are a combination of reflectances from several surrounding pixels, or even nearly no pixels at all (as is the case without high relative error pixel). When the emulator predicts the reflectance of this scene, shown in Fig 2.11 (d), the parallax should have already been corrected, meaning it predicts a much higher reflectance than exists in the "truth" scene, as it bases it on the cloud properties of that pixel. The very high relative error is also driven by the fact that the true reflectance in this scene is near-zero, which mathematically increases relative error due to the inverse relationship between relative error and the true value. Thus, this scene provides an example

of why the parallax correction for certain types of scenes creates very high relative errors for some pixels, increasing the standard deviation of the emulator accuracy and leading to very high kurtosis.

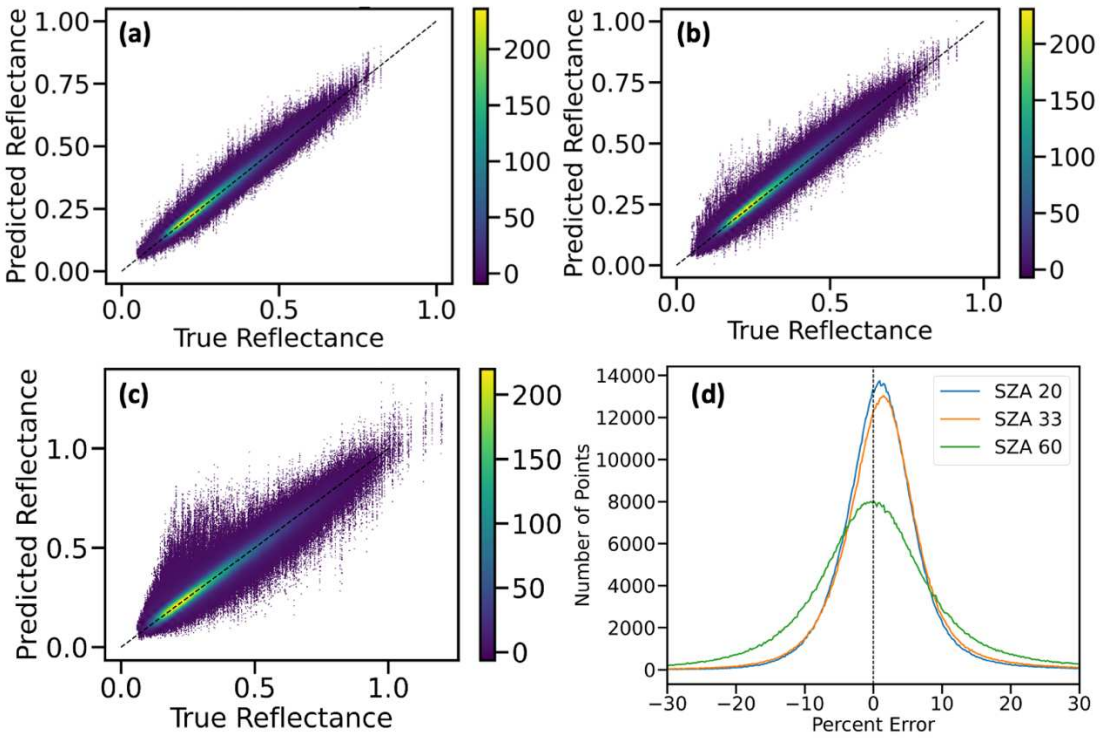

Figure 2.12. Scatter plots of the predicted vs. truth reflectance at 645 nm wavelengths for cloudy pixels, using emulators with a nadir viewing angle and solar zenith angle of (a) 20°, (b) 33°, and (c) 60°. The black dashed line shows the 1:1 line. (d) shows the histograms of the corresponding relative errors (%).

To further evaluate the impact of errors due to parallax corrections, we trained three emulators with a nadir viewing, where no parallax corrections are needed. These emulators were trained at three solar zenith angles of 20°, 33° (the same solar geometry as our VOCALS-REx case), and 60°. As expected, the scatter plots in Fig. 2.12 show that fewer data points deviated from the 1:1 line, indicating that the emulators generally perform better for the case of nadir-viewing compared to that of off-nadir viewing, except at SZA of 60°. As shown in Fig. 2.13, using the same scene as Fig. 2.11, the emulator works well in the absence of parallax effects. Comparing the error statistics at 645 nm in Table 2.4 between the 3rd and 4th set of the sun-viewing geometry

(i.e., nadir vs. off-nadir viewing angle), we see that the mean relative errors are comparable and the errors for the 15th, 50th and 85th percentiles are generally smaller in the case of the nadir viewing. The biggest differences are found in the standard deviation and Kurtosis, which are approximately doubled in the case of the off-nadir viewing. This suggests that the imperfect parallax corrections can lead to extreme relative errors, but the corrections are appropriate for most data points as shown by the similar statistics in other metrics.

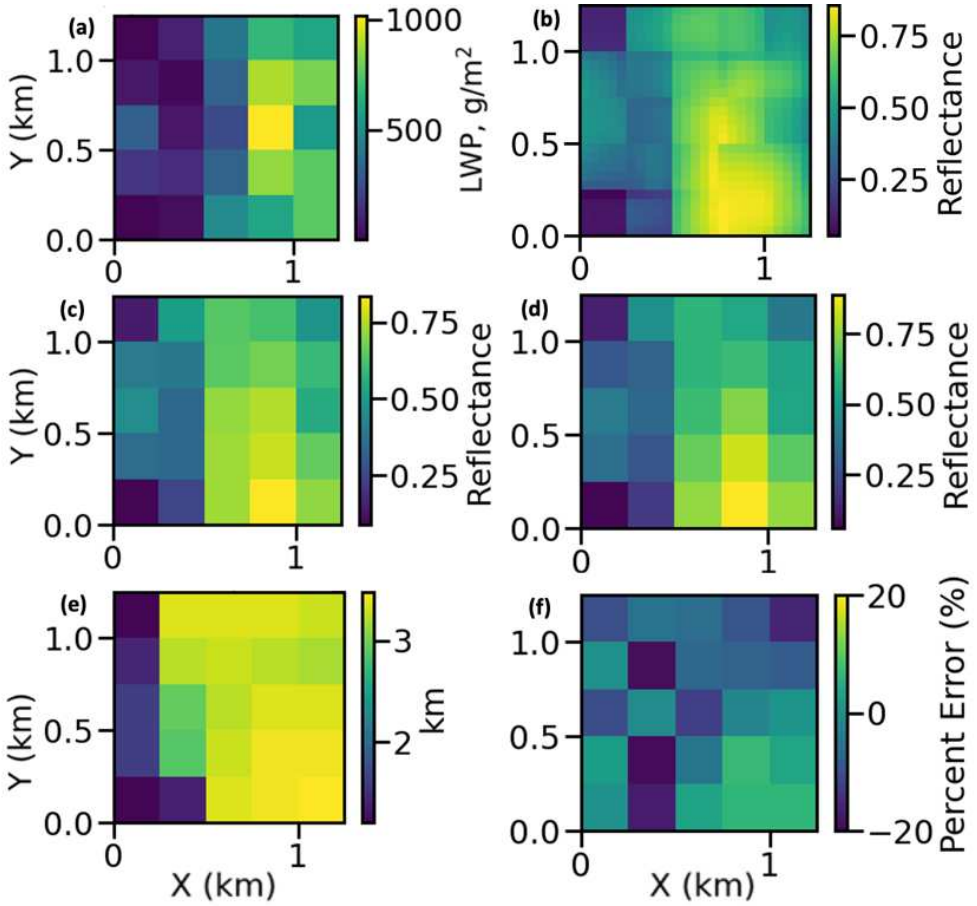

Figure 2.13. Same as Fig. 2.11, but for nadir-viewing.

The relatively poor performance of the emulator for SZA of 60° warrants further investigations. Figure 2.14 provides an example for illustrating the potential issue with emulations at large SZA. As shown in Fig. 2.14 (a) and (b), there is an optically thick and geometrically tall cloud at X = 0–1 km. This cast a shadow in both the buffer and core domains. Since our input

domain is small and does not include information on this big cloud and thus is not aware of the shadow effects, the predicted reflectance is generally too high compared to the truth (see Fig. 2.14 (c) and (d)), leading to a larger error compared to the case with small SZAs. To alleviate this issue, the size of the buffer domain needs to increase, but this may not be practical because it may also increase the size of state variables that need to be retrieved.

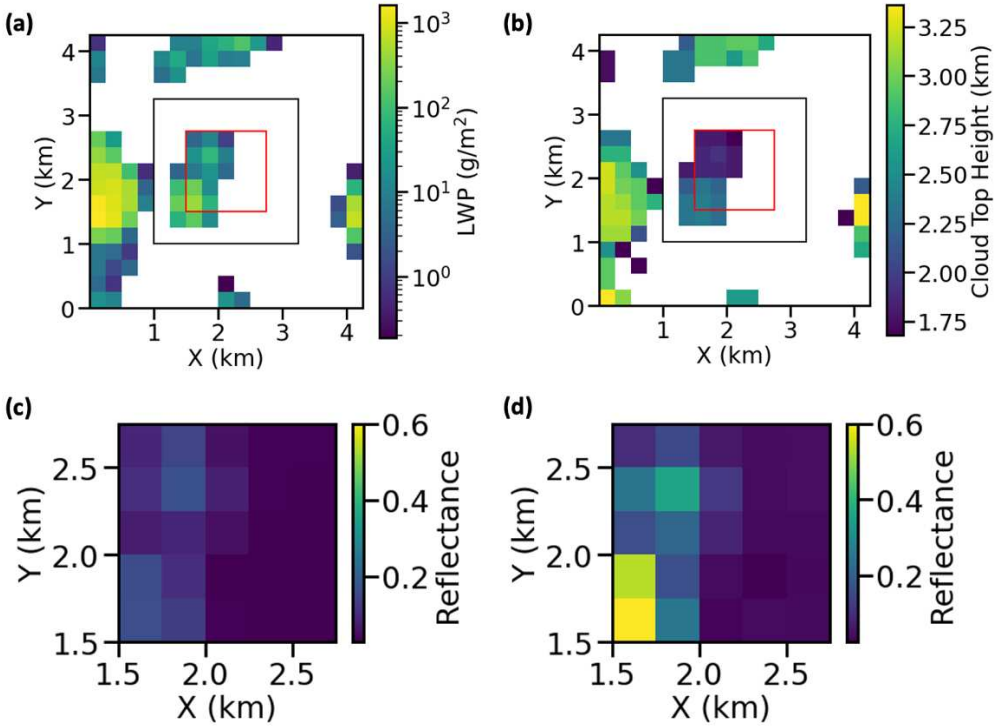

Figure. 2.14. An example of cloud scene for illustrating the potential source of errors for the emulator prediction at solar zenith angle of 60°, solar azimuth angle of 270°, and nadir viewing angle (i.e., the 2nd set of sun-viewing geometry in Table 2.3). (a) and (b) show the liquid water path and cloud top height over a larger domain than the buffer domain (represented by the black square box) and the core domain (represented by the red box). (c) and (d) show the truth and predicted reflectance at 645 nm over the core domain.

2.2.3 Evaluation using I3RC dataset

Thus far, our evaluation of these emulators has been limited to cloud scenes from LASSO. To further evaluate their performance, we tested a cloud scene from the international Intercomparison of 3D Radiation Codes (I3RC) project, which is funded by ARM and the NASA

Radiation Sciences Program and provides benchmarks for creating and testing 3D radiative transfer codes (Cahalan et al., 2005). The project also produced cloud scenes for testing, including a simulated stratocumulus cloud field. This dataset provided the LWC and r_e over a 3.52 km x 3.52 km domain with 55 m x 55 m x 25 m resolution. As shown in Fig. 2.15. (a), the scene was first expanded to allow us to test as many scenes as possible. Then it was interpolated into 250 m x 250 m x 60 m resolution to match the resolution of the emulator, as shown in Fig. 2.15 (b). Radiative transfer was then performed on this dataset using SHDOM to generate the synthetic truth for testing the emulators. This evaluation was performed at 645 nm wavelength with the sun-viewing geometry of the VOCALS-REx case.

When testing this I3RC case, Fig. 2.16 (a) shows that the emulator has an error standard deviation of 50% for cloudy pixels, which is much larger than expected compared to other emulators. We found that the large prediction errors are due to the cloud top height of the I3RC cloud field. Using a height-distance plot, Fig. 2.16 (b) shows that clouds are located between ~0.6 and ~0.8 km. Recall that the majority of cloud scenes have a cloud top height greater than 1 km in the training dataset (see Fig. 2.3 (a)). The I3RC case has a much lower cloud boundaries, which led us to understand some important behavior of our emulator as discussed next.

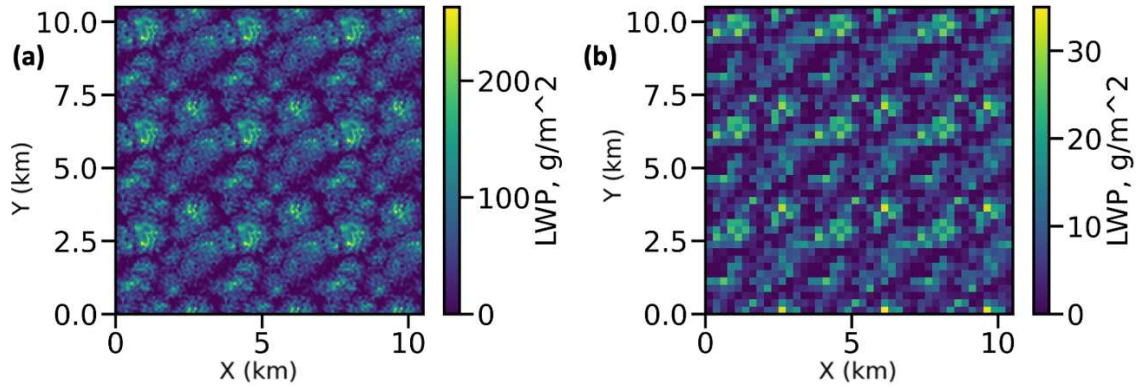

Figure 2.15. I3RC stratocumulus cloud scene with (a) original 55m x 55m x 25 m resolution and (b) interpolated to 250 m x 250 m x 60 m resolution.

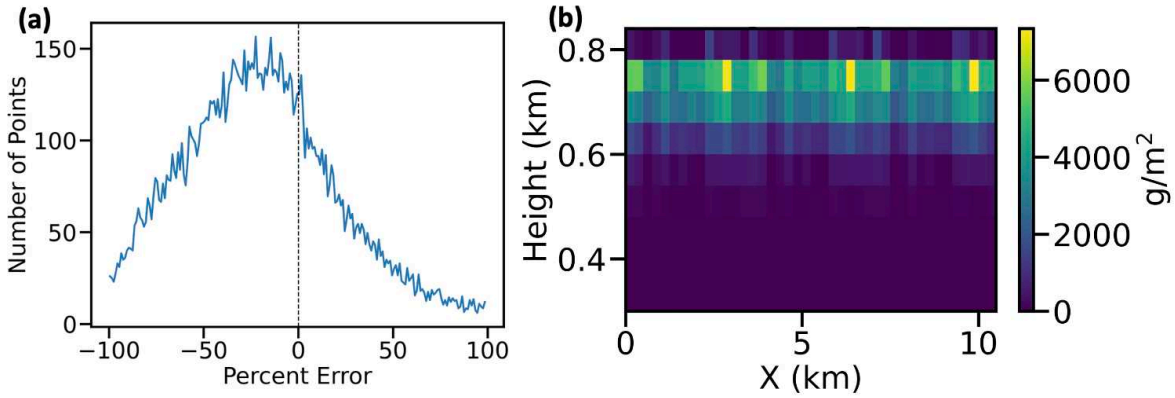

Figure 2.16. (a) A histogram of relative error (%) in reflectance at 645 nm for cloud pixels for the I3RC case, using the emulator with the sun-viewing geometry of the VOCALS-REx case. (b) A plot of height vs. liquid water path integrated along the y-direction in the I3RC case.

We found that the emulator performance depends on the locations of the input cloud layers. Using a cloud scene with a geometric thickness of 700 m from the validation dataset, we moved the clouds from their original cloud top height of 2.4 km to different heights and examined the corresponding performance. Figure 2.17 (a) shows that if the cloud top heights remain in the range between 1 and 4 km, the emulator has good performance with a mean relative error close to zero. However, if the cloud top height is outside this range, the performance degrades because of fewer samples in the training dataset as shown in Fig. 2.17(b).

Thus, the cloud layer in the I3RC scene is too low for the emulator to produce accurate results. Instead, if the I3RC scene was raised from 0.8 km to a cloud top height of 1.3 km, then the predicted reflectance from the emulator is far more accurate. As shown in Fig. 2.18 and Table 2.5, the histogram of the percent error for cloudy pixels and the error statistics are now comparable to the results in the testing dataset, although the errors are generally larger in the I3RC case. The degraded performance in the I3RC case may be due to the following reason. As shown in Fig. 2.19, the distribution of LWC and r_e is quite different between the datasets, likely leading to such

different performances. The histogram of LWC values present within the I3RC field extends to much higher values than the LASSO LWC values, meaning there is very little coverage within the training dataset for many values within LASSO. The LASSO histogram is also highly skewed towards zero, likely due to the interpolation of smaller cloud patches which get averaged with zero values nearby. The r_e value histograms also have quite different distributions, although the I3RC effective radii values are better covered within the training dataset than the LWC values. These differences are likely the drivers of the observed differences in emulator performance rather than issues with parallax shifts.

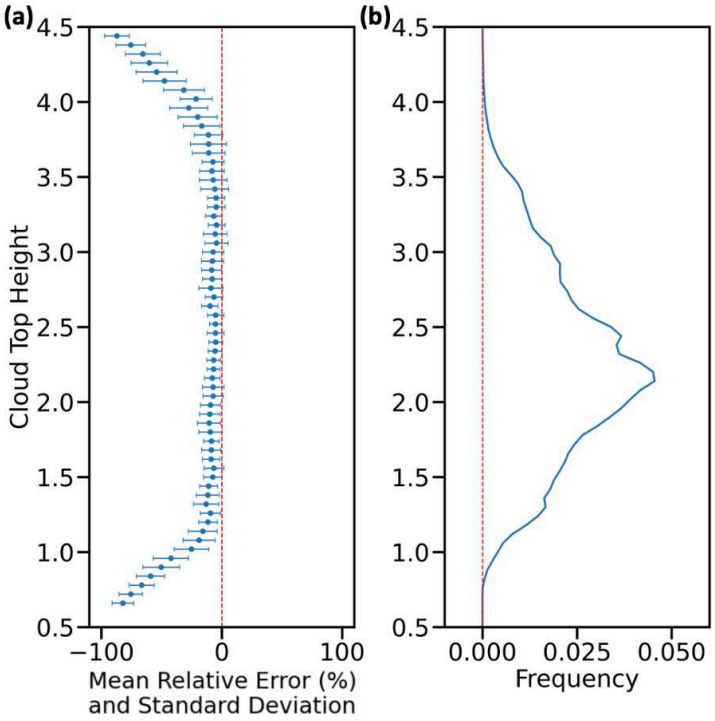

Figure 2.17. (a) Emulator performance at various altitudes using a cloud scene from the validation dataset. The mean percent error and the standard deviation of errors for cloudy pixels are represented by the dot and error bar, respectively. (b) Histogram of frequency of cloud top heights in the training dataset.

Table 2.5. Same as Table 2.4, but only including the error statistics from the emulator with the sun-viewing geometry of the VOCALS-REx case and the I3RC case with a raised cloud field.

Dataset	μ_E	σ_E	MAD	K_E	15th	50th	85th
Testing	1.0	14.1	8.2	77	–8.4	–0.3	8.9
I3RC	3.4	18.8	12.8	15	–11.5	1.2	17.7

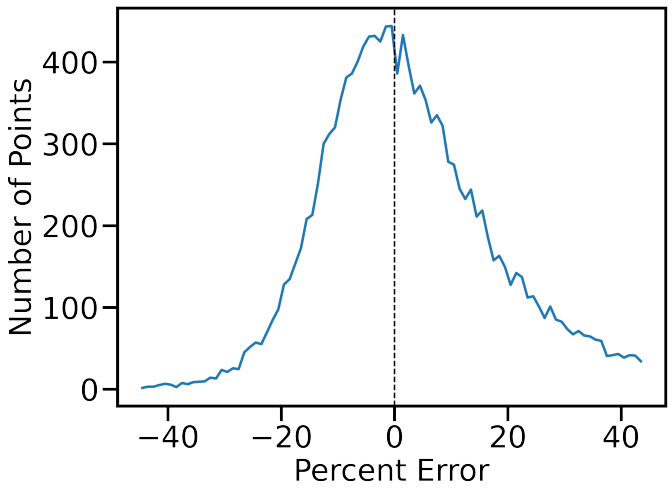

Figure 2.18. Histogram of the relative error (%) in predicted reflectance at 645 nm for the cloudy pixels in the I3RC case with a raised cloud field. The sun-viewing geometry is based on the VOCALS-REx case. Detailed error statistics can be found in Table 2.5.

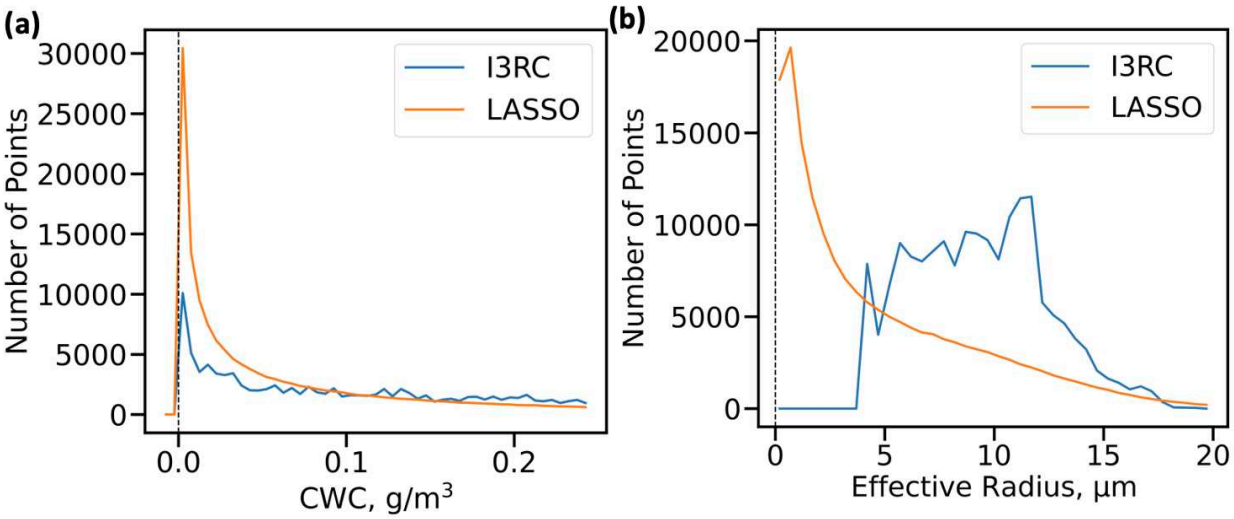

Figure 2.19. Comparison of cloud microphysical property frequency between I3RC and LASSO datasets. Note that the number of points has been normalized so they are equivalent. (a) Frequency of LWC values. The distribution is largely similar, but the I3RC case is more likely to have much larger values. (b) Frequency of r_e values. The I3RC dataset generally has significantly larger values.

In summary, the evaluation against the I3RC case indicates that the input cloud scene needs to have similar cloud heights to the testing dataset to achieve good predictions of reflectance at TOA. If clouds are too low in the scene, one way to alleviate the issue is to elevate cloud base heights. For the shortwave spectral region, the elevation of cloud height does not change reflectance significantly, because the reflectance is largely determined by cloud optical depth and droplet size rather than the height. However, a better way to resolve this issue is to expand the training database, which is possible since LASSO activity has been planned to extend their simulations for the ARM Eastern North Atlantic site at the Azores for marine boundary layer clouds.

CHAPTER 3: CLOUD OBSERVATIONS DURING VOCALS-REX CAMPAIGN

The emulator introduced in Chapter 2 is designed to predict reflectance measured from MODIS on the Aqua satellite, part of the A-Train. In this section, we detail A-Train observations that will be used for the retrieval method, focusing on a case observed during the VOCALS-REx campaign. In-situ cloud probe measurements from one of the VOCALS-REx research flights are presented to provide a context for A-Train observations.

3.1. VOCALS-REx observations

The VOCALS-REx campaign focused on improving understanding and modeling of the climate system over the southeast Pacific. This region is characterized by cold sea surface temperatures, strong coastal ocean upwelling, and the largest subtropical stratocumulus cloud deck on the planet. Significant anthropogenic pollutants originating on the coast of Chile modulate cloud properties and evolution and introduce uncertainties in climate sensitivity. The VOCALS-REx campaign, beginning in 2008, sought to reduce the systemic errors in global climate models at this time over this region and improve estimates of aerosol effects on low clouds and climate. The study involved field campaigns, buoy monitoring, and ship observations to compare to model outputs (Mechoso et al., 2014), as shown in Fig. 3.1.

Aircraft sampling was primarily concentrated along 20°S from the Chilean coast, which intersects the heart of the stratocumulus deck, while aircraft pollution survey missions extended south towards Santiago, Chile to sample the large anthropogenic aerosol plume. These missions occurred between 15 October and 15 November 2008. Among various research flights, we will focus on Flight #12 on 11 November 2008 because the flight track intersected and was temporally

close enough to the CloudSat track to allow for observation synergy. Although this flight was named a pollution survey, it contains extensive periods of cloud measurements. The geographical and temporal relationships between the VOCALS-REx flight, CloudSat and MODIS paths are shown in Fig. 3.2.

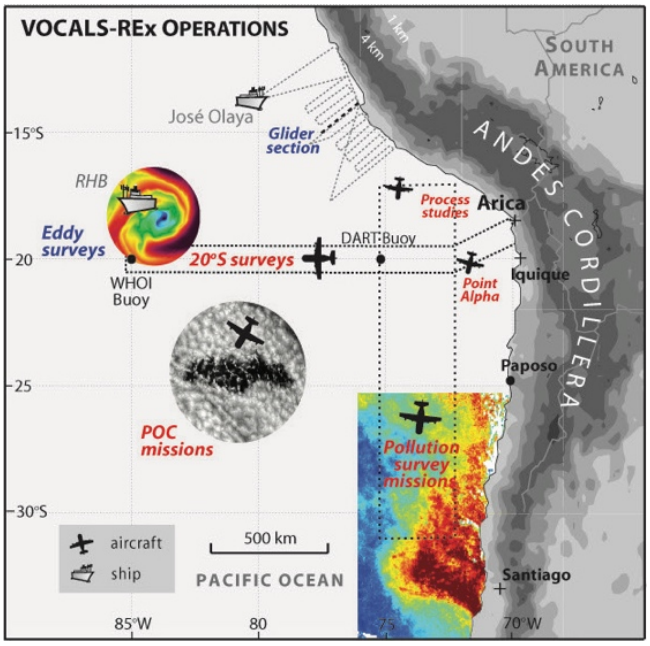

Figure. 3.1. Schematic of VOCALS-REx field campaign and the types of surveys included. Taken from Mechoso et al. (2014).

Measurements from three instruments during the VOCALS-REx Flight #12 are used to derive cloud microphysical properties. Liquid water content (LWC) was directly measured from the King hot wire probe (King et al., 1978). The probe does not suffer from drop size errors introduced by optical probes, making it useful to determine the bias of the other probes (Painemal and Zuidema, 2011). Cloud droplet size distributions (DSD) were measured from several probes, including the Cloud Droplet Probe (CDP) that measures droplet diameters in the 2–52 μm size range, and the Two-Dimensional Cloud optical array probe (2DC) that measures droplet diameters in the 25–1560 μm size range. Following Painemal and Zuidema (2011), we classified droplets

measured by CDP as cloud droplets and droplets measured by 2DC in the size bins that are not overlapped with CDP as drizzle drops.

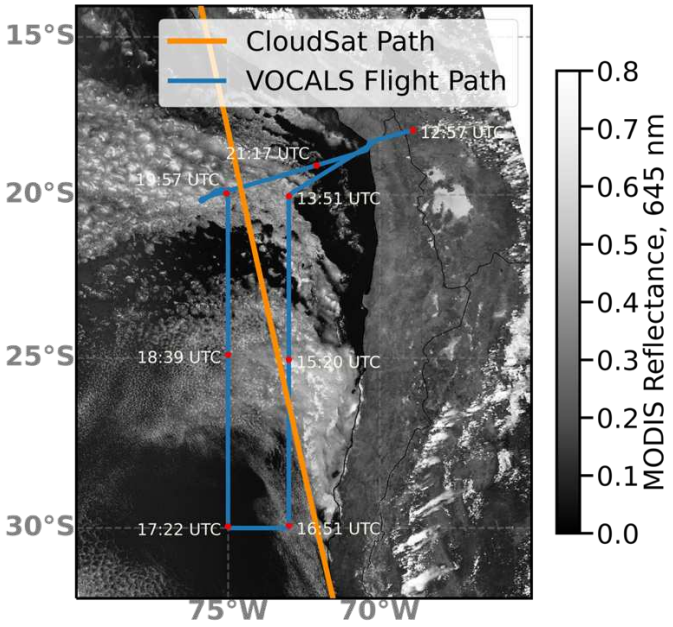

Figure 3.2. Background information for the VOCALS-REx Research Flight #12 on 11 November 2008, taking place off the west coast of northern Chile in the Pacific Ocean. The MODIS reflectance at 645 nm is shown in the background as grey scale, where stratocumulus cloud decks are visible over the ocean. The CloudSat track is shown in orange, and the overpass took place between 18:55 and 19:00 UTC. The VOCALS-REx flight path is shown in blue, with various time stamps of the flight labeled with red bullet points.

The DSD from CDP can be used to derive the total number concentration (N_c), LWC and effective radius (r_e), using the following equations:

$$N_c = \sum_{i=1}^{30} n_i, \tag{3.1}$$

$$\mathrm{LWC} = \frac{4\pi}{3}\rho_w \sum_{i=1}^{30} n_i \cdot r_i^3, \tag{3.2}$$

$$r_e = \sum_{i=1}^{30} r_i^3 \cdot n_i \Big/ \sum_{i=1}^{30} r_i^2 \cdot n_i, \tag{3.3}$$

where ρ_w is water density, n_i is the number of droplets per bin (# cm^{-3}), i is the bin (30 bins total), and r_i is the center bin radius. We define a cloudy sample as when LWC $\geq$ 0.01 g m^{-3}.

CDP and 2DC are useful as they can separate cloud and drizzle properties,and can be used to determine all microphysical properties, but CDP has a flight-dependent bias in which it oversizes droplets (Painemal & Zuidema, 2011). By taking a linear regression, a linear fit can be found, where $\mathrm{LWC_{CDP}} = a * \mathrm{LWC_{King}}$. Then, a is used to correct the CDP droplet size distribution by modifying the center radius of each bin, replacing r_i with $r_i^* = {r_i}/{a^{1/3}}$ (Painemal & Zuidema, 2011). In our flight, $a = 1.09$. The corrected CDP-calculated microphysical values are used for the remainder of the analysis.

Cloud properties sampled during the flight are shown in Fig. 3.3. As shown in Fig. 3.3 (a), the aircraft held a regular flight pattern, constantly moving up and down in altitude. With this altitude pattern, typically while ascending, it would quickly pass through the layer, and while descending, it would stay in the cloud for roughly 20–30 mins. The four periods of cloud measurements are shown in Fig. 3.4. This is useful as we have cloud profiles occurring at roughly the same horizontal location, and cloud transects for an extended distance (although only at one horizontal portion of the cloud layer). While cloud properties have some variation throughout the flight, r_e generally had relatively constant values of 3 μm to 8 μm (see Fig. 3.3 (d)), LWC ranged from 0.1 g m^{-3} to 0.35 g m^{-3} (see Fig. 3.3 (c)), and N_c ranged from 100 cm^{-3} to 350 cm^{-3}, although N_c was generally constant throughout each profile of the cloud layer (see Fig. 3.3 (b)). N_c was also higher when the aircraft was in the northern region of the cloud field; this region was more heavily influenced by anthropogenic aerosols originating off the coast of Chile.

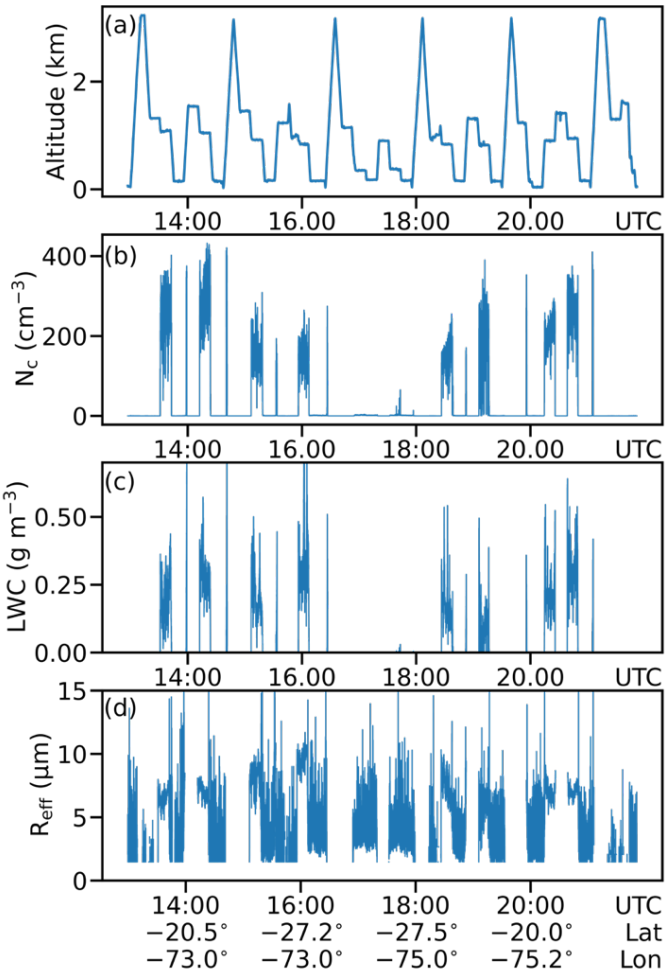

Figure 3.3. Time series of (1) aircraft height, (b) cloud droplet number concentration, (c) liquid water content, and (4) cloud effective radius observed during the flight of VOCALS-REx on 11 November 2008. The latitude, longitude, and timestamps for reference are shown at the bottom. All cloud properties plotted here were computed using droplet size distributions measured from CDP.

Following Painemal and Zuidema (2011), we used the cloud profile at UTC 18:45 identified in Fig. 3.4 to evaluate how adiabatic the cloud field was. The adiabatic growth rate (Γ_{ad}) of liquid water content is a function of temperature and pressure. For this region, the typical range of Γ_{ad} is between 1.8 g m^{-3} km^{-1} and 2.2 g m^{-3} km^{-1} (Painemal and Zuidema, 2011). The measured LWC of this profile, along with the N_c profile and r_e profile, are shown in Fig. 3.5. As shown in Fig. 3.5 (a), the measured LWC profile matches better with the profile with Γ_{ad} of 2.0 g m^{-3} km^{-1}

multiplied by a sub-adiabatic fraction of 0.7, indicating this cloud field is not adiabatic. However, Painemal and Zuidema (2011) found that most profiles they analyzed were consistent with adiabatic expectations. Hence, the profile in Fig. 3.5 is likely an outlier. Moreover, Fig. 3.5 (b) shows that the N_c profile is somewhat vertically homogeneous, except near the cloud base and cloud top.

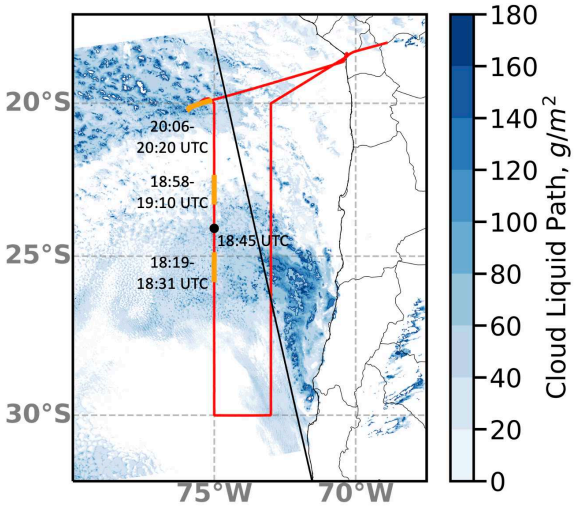

Figure. 3.4. The VOCALS-REx flight path is shown in red. Regions where the aircraft was in-cloud for an extended period within roughly 1 h of the A-Train overpass are shown in orange with timestamps. The black bullet point is the time and location of the vertical profile. The CloudSat path is shown in black, and MODIS retrieved cloud LWP is shown in blue. The A-Train overpass occurred between 18:55 and 19:00 UTC.

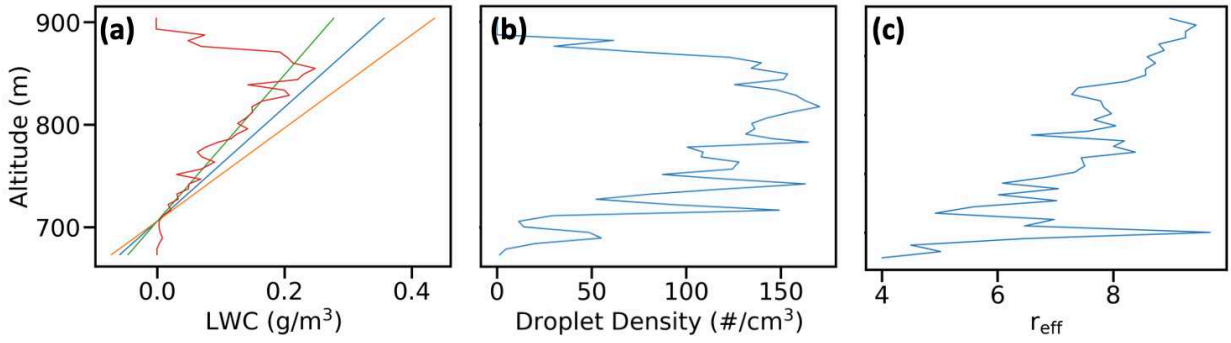

Figure 3.5. Profile of (a) liquid water content, (b) cloud droplet number concentration, and (c) cloud effective, based on CDP measurements at 18:45 UTC as marked in Fig. 3.4. In (a), LWC profiles calculated from three adiabatic growth rates (Γ_{ad}) are also shown, including Γ_{ad} of 1.8 g m^{-3} km^{-1} (blue), 2.2 g m^{-3} km^{-1} (orange), and 2.0 g m^{-3} km^{-1} with a sub-adiabatic fraction of 0.7 (green).

In the three periods highlighted in Fig. 3.4, the aircraft entered and exited the cloud layer at very different horizontal locations, meaning this method of analyzing cloud profile properties cannot be applied. The aircraft flight pattern was to enter the cloud top (or base), continue at a set altitude through the middle of the cloud layer, then exit the cloud base (or top). The box plot for the measurements at 18:19–18:31 UTC in Fig. 3.6 suggests similar ranges of cloud microphysical properties between the profiling transect and the horizontal transects. Overall, LWC increases with height and is up to ~0.3 g m^{-3}, N_c mainly ranges between 100 and 200 cm^{-3}, and r_e ranges between 5–10 μm.

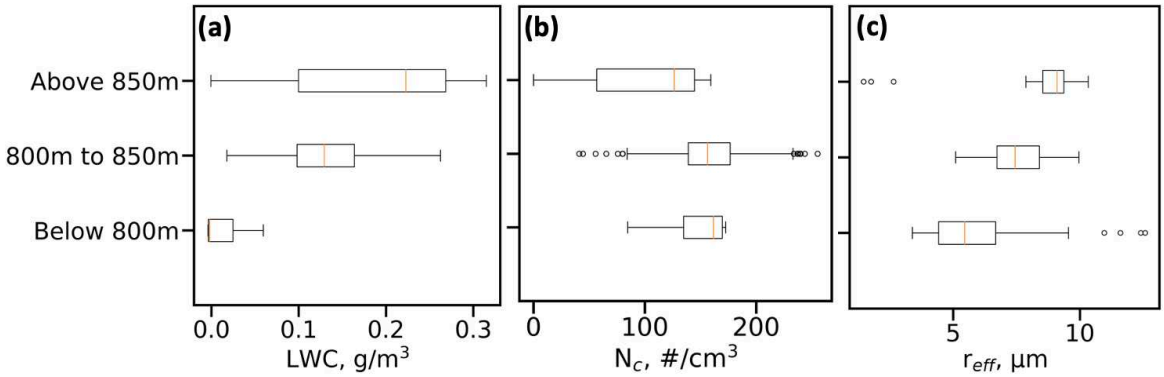

Figure 3.6. Boxplots of (a) liquid water content, (b) cloud droplet number concentration, and (c) cloud effective measured during the 18:19-18:31 UTC flight transect, using three altitude bins. The outliers are points outside the [Q1 – 1.5 IQR, Q3+1.5 IQR] margin, where Q1 and Q3 (first and third quartiles) are the 25th and 75th percentiles, respectively, and the IQR (interquartile range) = Q3-Q1. The cloud base height is 820 m, and the cloud top height is 925 m. The sample size for the three altitude bins from the lowest to the highest is 57, 645, and 23, respectively.

3.2. A-Train satellite observations

The retrieval method under development uses three sets of satellite observations: reflectance at three wavelengths from the Moderate Resolution Imaging Spectrometer (MODIS)

aboard the Aqua satellite, radar reflectivity profiles from the Cloud Profiling Radar (CPR) aboard CloudSat (Stephens et al., 2002), and lidar backscattering from Cloud-Aerosol Lidar and Infrared Pathfinder Satellite Observation (CALIPSO; Winker et al., 2007). These are part of the NASA A-train satellite constellation, which fly in close proximity to each other in a sun-synchronous polar orbit at an altitude of 705 km with an equator-crossing time of 1:30 PM. Aqua is the lead constellation spacecraft, followed by CloudSat with a variable interval of up to 120 s, which is followed by CALIPSO at an interval of about 15 s (Stephens et al., 2002). An example of the MODIS reflectances and the CloudSat track for the VOCALS-REx case of Research flight 12 is shown in Fig. 3.2.

MODIS measures reflected solar and infrared radiation at 36 channels between 405 nm and 14 μm at resolutions between 250 m and 1 km. We use reflectance at three wavelengths: 645 nm, 857 nm, and 2113 nm. To minimize the errors introduced by ignoring sub-pixel cloud variability (see Section 1.3), we use the MODIS Level 1B product (MYD02QKM) that provides calibrated radiances and reflectance at the finest horizontal resolution of 250 m that MODIS offers.

CPR operates at 95 GHz with a 2 km resolution along-track and 1 km resolution across-track. Radar reflectivity measurements have a vertical resolution of 480 m, although they are oversampled at 240 m. The minimum detectable radar reflectivity is about –30 dBZ (Marchand et al., 2008), at which point the radar noise power equals the return power. To be scientifically useful, the hydrometeor signal must be separated from the noise, which combine to create the measured raw return power (Hu et al., 2020). Thus, CloudSat provides a "cloud mask," which provides the statistical likelihood a cloud exists within a cloud bin, which is provided in the 2B-GEOPROF cloud mask product. A cloud mask value of 20 was used, which has a higher uncertainty of the cloud presence than 30 or 40, but the use of more restrictive masks leads to very few cloudy pixels.

The primary challenge for our case study is surface clutter, which makes CloudSat cloud measurements near the surface difficult because the outgoing radar pulse has a finite rise time rather than being a perfect square wave. The surface is several orders of magnitude more reflective than hydrometeors, and surface clutter extends up to the fourth 240 m bin above the surface (Marchand et al., 2008). Moreover, CPR has a sensitivity of about -30 dBZ, meaning non-drizzling marine low clouds would be very challenging to detect (Marchand et al., 2008). This means that marine low clouds may not be identified robustly by CloudSat. Figure 3.7 shows an example along latitudes between –20° and –30°. If only gates with cloud mask values equal to or greater than 20 are used, we see that the threshold of cloud mask may be too conservative. Additionally, VOCALS-REx in-situ observations show a typical cloud base of 0.5–0.8 km, suggesting that many cloudy gates below 0.7 km may have been missed in Fig. 3.7.

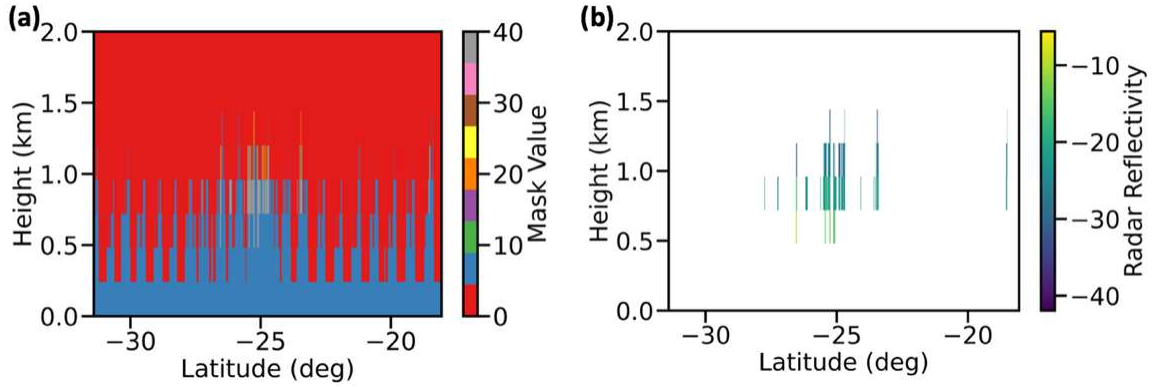

Figure 3.7. (a) Heigh-latitude plot of CloudSat cloud mask along the CloudSat track for the VOCALS-REx case. A mask value of at least 10 indicates a cloud, and values of 20, 30, and 40 each indicate a greater likelihood that a cloud exists. (b) The radar reflectivity of regions with a cloud mask value of at least 20.

CALIOP measures backscatter at 532 nm and 1064 nm with a horizontal spatial resolution of 333 m and a vertical resolution of 30 m. This provides direct vertical distributions of clouds and aerosols using polarization-sensitive elastic backscatter lidar. The measured backscatter intensity

is either air molecules (V_m) alone or a combination of air molecules and particulates (V_{m+p}). These are separated by a threshold (V_T), where signals above V_T are assumed to contain both air molecules and particulates. In reality, these two signals can overlap, leading to missed features and false positives, but the probability of successful detection can be increased by applying additional signal averaging. One key advantage of CALIPSO lidar over CloudSat radar is that, although the surface signal is visible at 0 km, that signal does not affect the layers above it, meaning surface clutter is not an issue. One disadvantage is that lidar has much stronger attenuation than radar, especially in clouds, meaning CALIPSO is often unable to determine the cloud base height, even for relatively thin clouds (Vaughan et al., 2009). As CloudSat and CALIPSO fly in formation, many products merge the datasets, allowing the advantages of each to complement one another.

An algorithm called DARDAR-CLOUD V2 (raDAR/liDAR), developed by Laboratoire Atmosphères, Milieux, Observations Spatiales (LATMOS) and the University of Reading in Cazenave et al. (2019), combined CPR and CALIOP measurements and provides target classifications at a horizontal resolution of 1.1 km and vertical resolution of 60 m. Considering the small geometrical thickness of marine low clouds, the much finer resolution of DARDAR products is particularly beneficial to our study. An optimal estimation algorithm is used to find the state vector for cloud properties which minimizes the errors on the observed radar reflectivity and lidar backscatter when compared to simulated measurements using a forward model. If one measurement is missing, an a priori estimate of the state vector is derived from the climatology. To provide a snapshot view, Fig 3.8 shows the classifications from the standard CloudSat product and DARDAR. Clearly, incorporating lidar signals helps detect relatively thin clouds and low, providing more radar reflectivity profiles for one to perform the donor-recipient match.

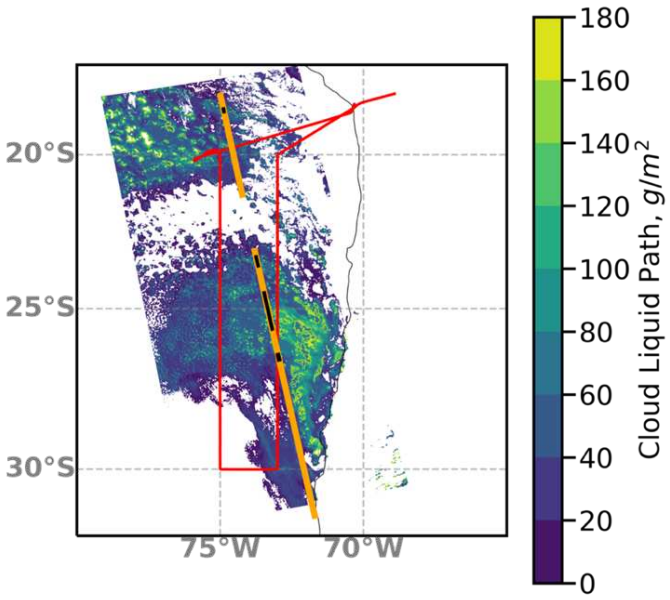

Figure 3.8. Comparison of regions where clouds were detected by different cloud products. The CloudSat 2B-GEOPROF product is shown as the black line. The DARDAR product is shown as the orange line. The VOCALS-REx flight path is shown in red for reference. The background is LWP derived from the MODIS MYD06_L2 cloud product.

Using the same example as Fig. 3.7, the cloud mask and radar reflectivity from the DARDAR product are shown in Fig. 3.9. The horizontal extent of the cloud layer is much larger and more consistent with the location of clouds in the MODIS image and VOCALS-REx cloud statistics in terms of cloud top height at around 1 km. However, several issues remained. First, as seen in the cloud mask, there are many small vertical sections labeled “liquid warm cloud” above the more dominant piece of cloud. It was important to identify whether this was a misclassification within the cloud product or a true section of cloud. Second, the gaps between these “clouds” and the main layer also presents an issue, as our current retrieval method is designed to apply to single layer clouds. Moreover, the VOCALS-Rex measurements show that cloud tops are typically below 1 km, and thus the clouds above 1 km are likely misclassified. In the main cloud layer itself, some pixels are labeled “don’t know” between pixels labeled “liquid warm cloud”. Finally, from Fig.

3.9 (b), we can see that there are many gates which are labeled “liquid warm cloud” which do not actually contain any radar reflectivity information, as the field is left as 0 mm^6/m^3.

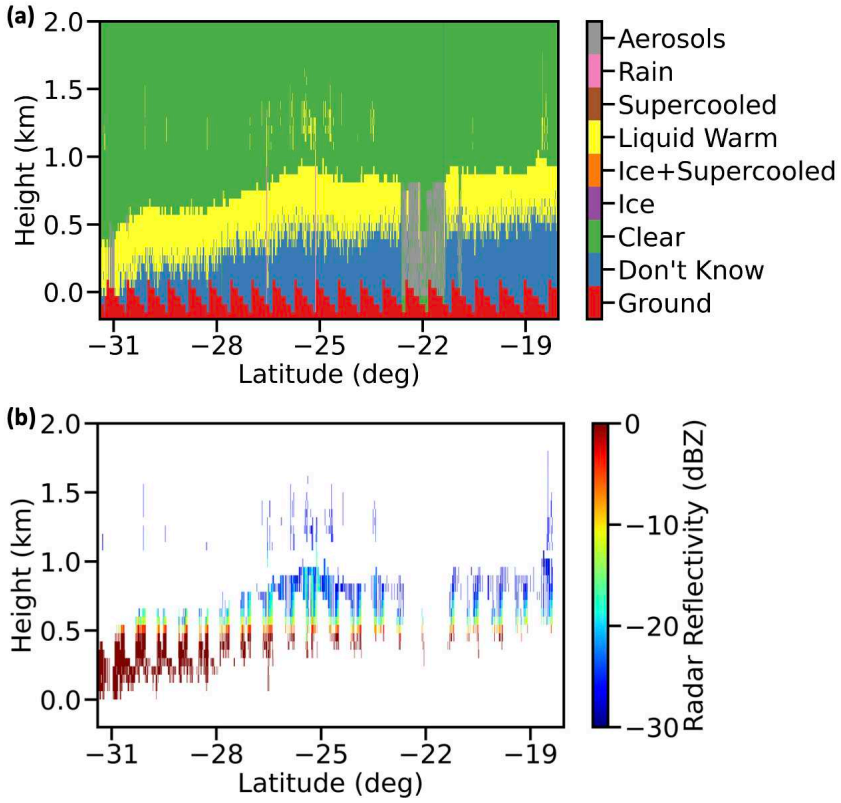

Figure 3.9. (a) Cloud mask and (b) radar reflectivity from DARDAR for the same CloudSat track used in Fig. 3.7. Many regions where are labeled “liquid warm” have invalid radar reflectivity and have been left as blank in the figure.

To address these issues, we made several alterations to the DARDAR cloud mask. To determine whether the high cloud pixels were misclassified, we plotted the lidar attenuated backscatter in relation to the radar reflectivity field, shown in Fig. 3.10. Here, the backscatter is masked to a threshold of 0.0001 $m^{-1}sr^{-1}$, above which there is a cloud signal, and below which there is a background signal. From this, we can assume the true cloud top is the lower section of the cloud, allowing us to modify the mask such that cloud pixels above this lidar attenuated backscatter are clear. Next, we filled in the gaps which exist in certain profiles within the cloud

layer by reassigning gates with the "don't know" mask as "liquid warm." The new mask is shown in Fig. 3.11 (a).

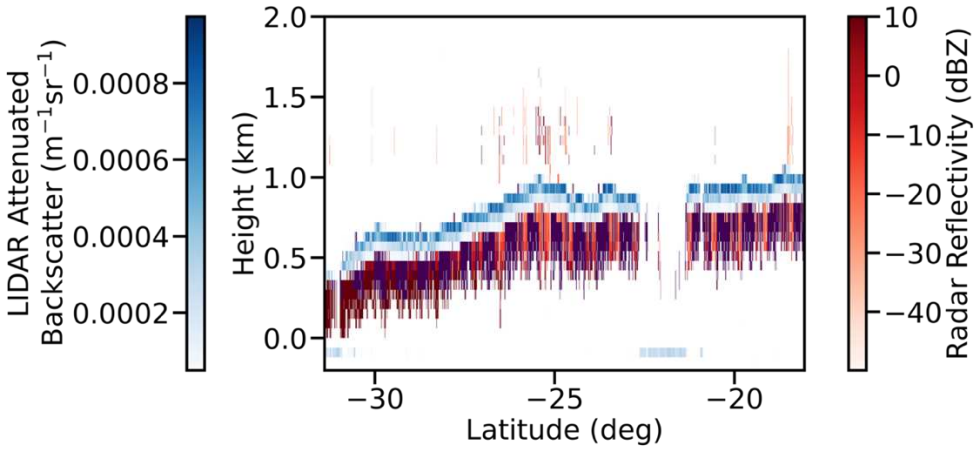

Figure 3.10. DARDAR radar reflectivity product masked to liquid warm clouds. Radar reflectivity is shown in red and regions where the radar reflectivity was 0 mm^6/m^3 are shown as dark purple. The lidar attenuated backscatter, masked to pixels greater than 0.0001 m^{-1} sr^{-1}, is shown in blue.

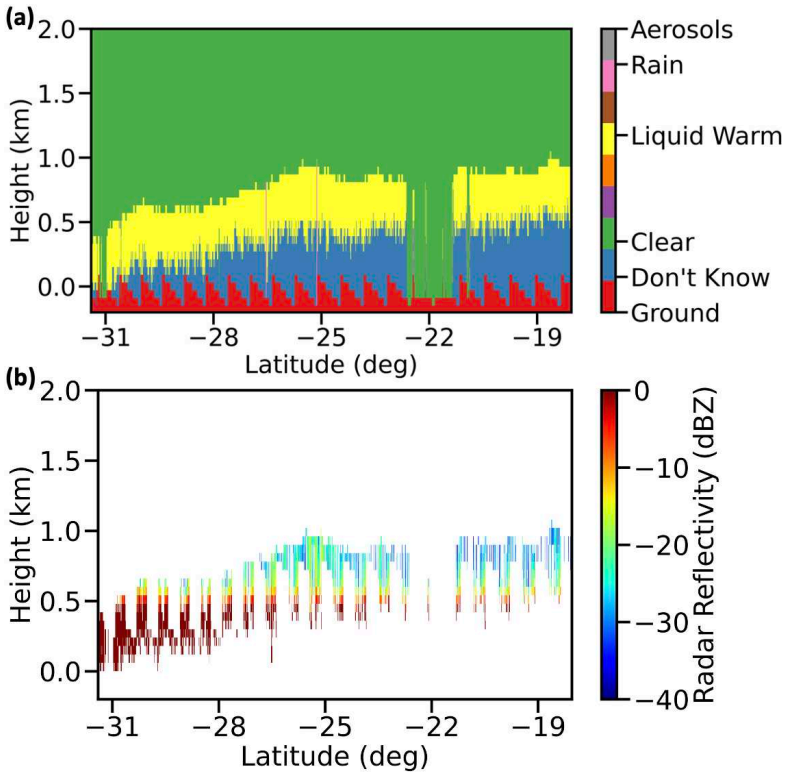

Figure 3.11. (a) DARDAR cloud mask after removing cloud pixels above the lidar signal and filling in gaps within the cloud. Note that because all features above the lidar signal were classified "clear", some features such as the aerosol plume have not been preserved. The intent of this mask is only to accurately create the cloud portion of the mask. (b) Radar reflectivity masked to this new cloud mask.

CHAPTER 4: COMPARISONS BETWEEN 1D and 3D CLOUD RETRIEVALS USING SYNTHETIC DATA

Before applying the retrieval method under development to A-Train observations, we investigate the difference in errors between 1D and 3D retrievals using a synthetic dataset. Our synthetic dataset is based on simulations from the Environment and Climate Change Canada high-resolution Numerical Weather Prediction model, known as the Global Environmental Multiscale model (GEM). These simulations, provided by Howard Barker, were generated for testing retrievals that will be made from the future EarthCARE satellite mission (Qu et al., 2017). The simulations have a horizontal resolution of 250 m and a vertical resolution that ranges between 80 m at the surface and 420 m in the upper atmosphere. We have selected a 100 km x 100 km scene with inhomogeneous warm clouds, as shown in Fig. 4.1.

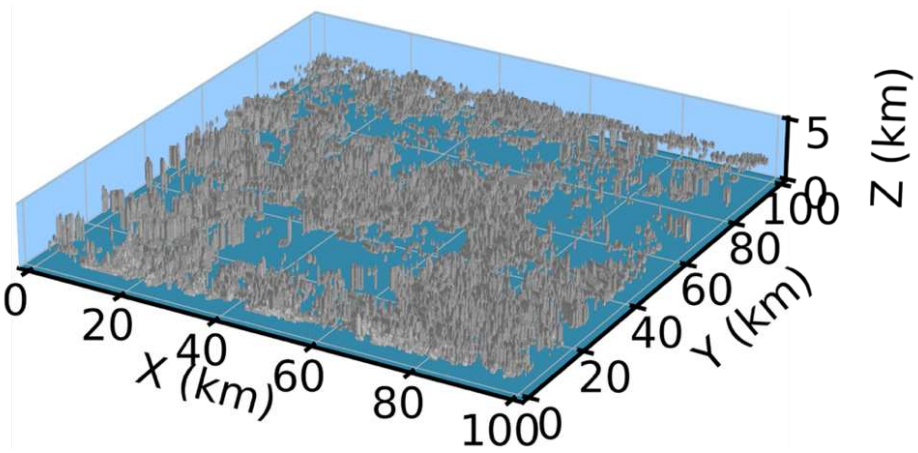

Figure 4.1. Overview of the entire synthetic cloud field, courtesy of Howard Barker. Shown in gray is the iso-surface where the cloud water content ≥ 0.01 g/m^3.

The synthetic reflectance was generated using the 3D version of SHDOM at wavelengths of 645 nm, 857 nm, and 2113 nm. The solar zenith angles were set as 20° and 60°, and the atmospheric conditions (including ambient aerosol properties) and surface albedo were set using

information from NASA Aerosol Robotic Network (AERONET) retrievals, MODIS aerosol retrievals, VOCALS-Rex aerosol measurements, and wind speed from European Center for Medium-Range Weather Forecast (ECMWF) Reanalysis v5 (ERA5) data. These conditions are the same as those used in training the emulators and can be found in section 2.1. The synthetic radar reflectivity is calculated using Quickbeam (Haynes et al., 2007), assuming a lognormal cloud DSD.

4.1. Analysis using 1D retrievals

We performed our retrieval using the 1D method discussed in Chapter 1.2. Following Nakajima & King (1990), lookup tables were generated using the DIScrete Ordinate Radiative Transfer (DISORT) (Stamnes et al., 1988) at 0.645 μm and 2.113 μm at two SZA of 20º and 60º. Our viewing zenith angle is at nadir. Using these lookup tables, which contain $4\ \mu m \leq r_e \leq 20\ \mu m$ and $1 \leq \tau \leq 100$, we retrieved the 1D τ and r_e, then compared the τ and LWP to the truth. We assume that liquid water content increases with height and thus retrieved LWP is calculated using $LWP = (2/3)\ \rho_w\ \tau\ r_e$. The intercomparison is performed for cloudy pixels only, defined as the cloud column that has at least one gate with LWC $\geq$ 0.01 g m^{-3}.

Scatter plots of these results are shown in Fig. 4.2, and the error statistics are listed in Table 4.1. As shown in the scatter plots, most retrieved LWP and τ are generally underestimated. The mean relative error of 1D optical depth retrievals is 55%, mainly due to pixels with small optical depths. Compared to Zinner & Mayer (2006), which reported a mean relative error of –5% for a case with a similar SZA, the error of 55% in our 1D retrievals is much larger. When excluding those optically thin pixels in the evaluation, the mean relative errors for τ and LWP are reduced to –5.6% and –1.4%, respectively. Since LWP is the product of retrieved τ and r_e, it typically has

smaller retrieval errors than those in τ because of possible compensating errors between τ and r_e. This feature is shown in the mean relative errors when excluding optically thin clouds, but not in the case with all pixels. Note that our lookup tables only contain optical depth up to 100 and r_e up to 20 μm. Thus, by default, the retrieval method is unable to predict pixels with large LWP and τ.

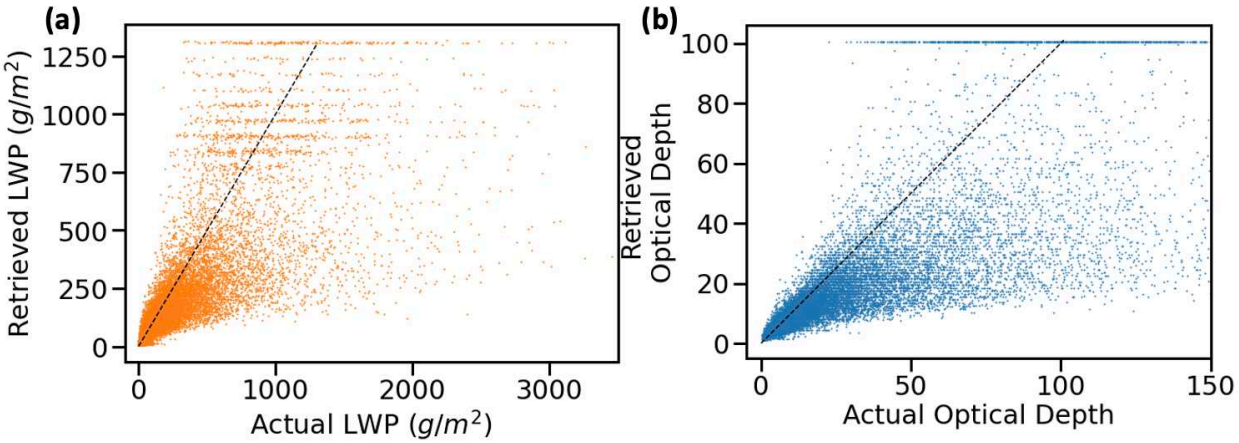

Figure 4.2. Scatter plots of the retrieved versus the truth (a) liquid water path and (b) cloud optical depth using the synthetic data. Retrievals are based on 1D radiative transfer at SZA of 20º. The 1:1 line is shown as dashed black. The maximum retrievable τ is 100 as that is the extent of our lookup table.

Table 4.1. Mean and standard deviation of errors (%) of pixel-by-pixel retrieved properties for the case with SZA of 20º.

Property	Percent error, all pixels	Percent error, only $\tau > 2$	Absolute error, all pixels	Absolute error, only $\tau > 2$
τ	55 ± 101%	–5.6 ± 38.2%	–4.3 ± 19.1	–7.9 ± 23.4
LWP	109 ± 210%	–1.4 ± 55.0%	(–30 ± 169) g m^{-2}	(–53 ± 209) g m^{-2}

The same analysis was performed on the SZA = 60º case, and the error statistics can be found in Table 4.2. Here, excluding pixels with low τ had a much less pronounced effect. Compared to Zinner & Mayer (2006), which reported mean errors of 50–100% and a standard deviation of ~80% in 1D retrieved τ, our 1D retrieval errors are similar at this geometry.

Table 4.2. Same as Table 4.1, but for the SZA = 60º case.

Property	Percent error, all pixels	Percent error, only $\tau > 2$	Absolute error, all pixels	Absolute error, only $\tau > 2$
τ	60 ± 86%	44 ± 100%	4.6 ± 21.9	6.8 ± 26.0
LWP	104 ± 184%	25 ± 80%	(–2.7 ± 179.5) g m^{-2}	(–9.1 ± 255.8) g m^{-2}

We can also quantify the effects of shadowing and illumination on 1D retrieved cloud properties by following Marshak et al. (2006). To define illuminated and shadowed pixels, in addition to 3D RT, we also performed 1D RT in SHDOM at the same wavelengths and geometry. Cloud pixels with a reflectance greater in the 3D RT than the 1D RT are deemed "illuminated" and those with a reflectance less in the 3D RT are deemed "shadowed." The retrieved τ and r_e values are then classified as "illuminated" or shadowed" so that the 3D effects on the retrieved properties can be quantified. An example portion of the subscene, highlighting illuminated and shadowed pixels, is shown in Fig. 4.3.

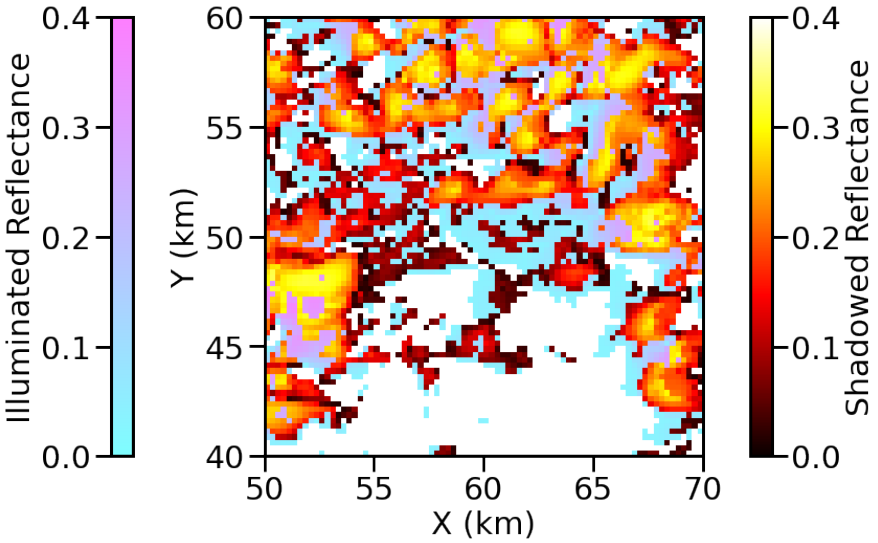

Figure. 4.3. Example portion of cloud scene at 645 nm with "illuminated" pixels shown as on a blue-pink color bar and "shadowed" pixels shown on a red-yellow color bar. SZA = 20º and SAA = 270º from north. Pictured is a sub-section of the cloud field in Fig. 4.1.

The shift in r_e and τ for each classification for the 20º case is shown in Fig. 4.5. The mean and standard deviation of the shifts for both solar zenith angles are shown in Table 4.3. The direction of the shift of τ is as expected, with the shift in τ of shadowed pixels $\Delta\tau_{shad} < 0$ and the shift in τ of illuminated pixels $\Delta\tau_{ill} > 0$, but the relative magnitude is not. $\Delta\tau_{ill}$ should be greater than $\Delta\tau_{shad}$ because of the shape of the function of τ against non-absorbing reflectance; an increase in reflectance will result in a much larger shift in retrieved τ than a decrease in reflectance of the same amount (Marshak et al., 2006). However, this assumes that equal amounts and magnitudes of shadowing and illumination are present. Our observed behavior is due to the skewed distribution of shadowing and illumination; at 20º, roughly three times as many pixels were illuminated as shadowed, and 86% of pixels with $\tau < 5$ are illuminated. Moreover, 79% of illuminated pixels have $\tau < 5$ and thus can only be shifted by a small amount. This can be seen in Fig. 4.4 (a), where most illuminated pixel optical depth shifts are less than 5. In contrast, shadowed pixels are primarily composed of very high optical depth pixels, where much larger optical depth shifts can occur.

The mean shift in r_e also has the expected signage, but not the relative magnitude, as observed $|\Delta r_{e,ill}| > |\Delta r_{e,shad}|$. Initially, effective radii shifts did not have a clean cutoff at 0. This was because a high number of our pixels had very low optical depths. At low τ, the r_e lines become so dense and steeply sloped relative to τ that finding the "nearest neighbor" within our lookup table (which is the first step in the lookup algorithm) can retrieve the incorrect r_e. This added substantial noise to the retrievals which was greater than the actual shifts due to 3D radiative effects. This could be addressed by removing r_e or adding τ values to our lookup table, but for this analysis, we constricted our analysis to pixels where $\tau > 20$, where the lookup table is orthogonal.

The results of the 60º were similar to the 20º case, but here $|\Delta\tau_{ill}| > |\Delta\tau_{shad}|$ as expected. This is because in the 60º case the vast majority of $\tau > 5$ pixels were shadowed, not illuminated, leading to the opposite behavior as the 20º case. In general, the IPA retrieval overestimated the τ across all values. The r_e shifts were more pronounced than in the 20º case, as 3D effects are more significant at higher solar zenith angles.

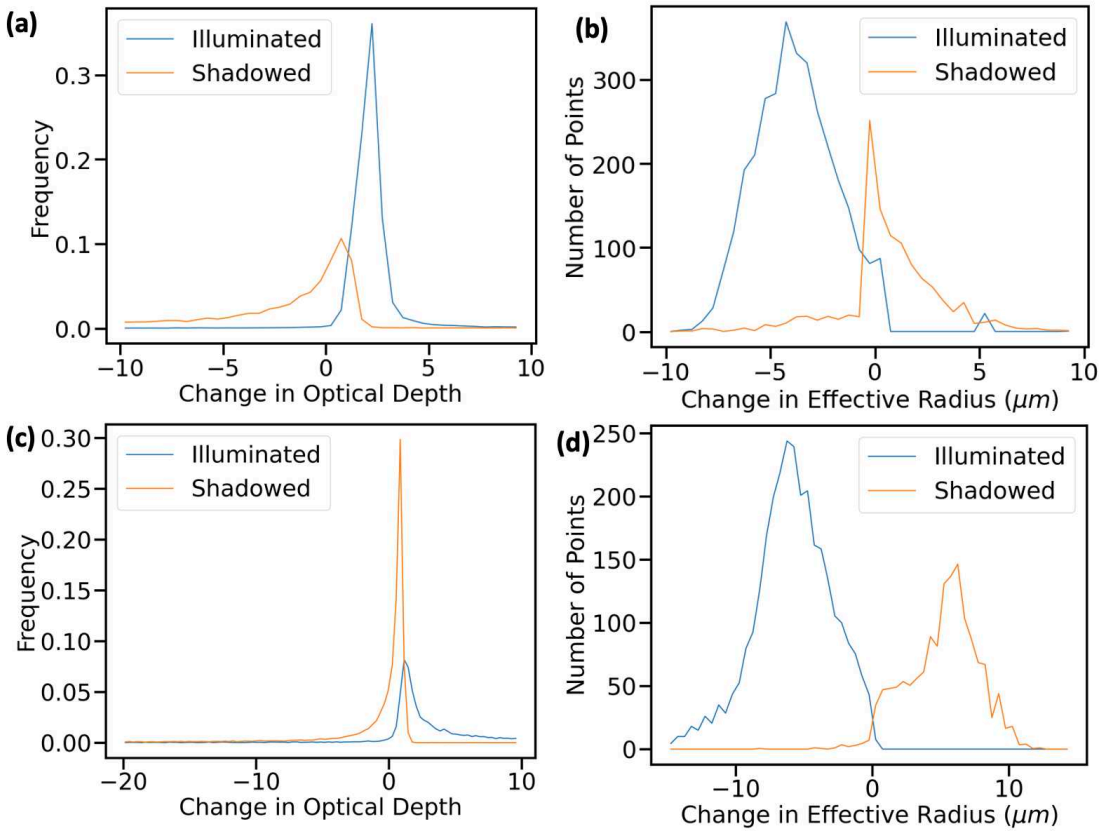

Figure 4.4. Histogram of difference between 3D retrieved properties and true properties for shadowed and illuminated pixel for (a) τ, SZA = 20º, (b) r_e, SZA = 20º, (c) τ, SZA = 60º, and (d) r_e, SZA = 60º. "True" r_e is the r_e of the highest cloud pixel within the column.

Table 4.3. Mean and standard deviation of shifts in cloud optical depth (τ) and effective radius (r_e) from truth for illuminated and shadowed pixels for both cases.

Case	$\Delta\tau_{\text{shad}}$	$\Delta\tau_{ill}$	$\Delta r_{\text{e,shad}}$ (μm)	$\Delta r_{\text{e,ill}}$ (μm)
20º	-12.3 ± 25.5	2.7 ± 5.9	0.8 ± 2.3	-3.8 ± 1.9
60º	-5.0 ± 19.4	12 ± 34	3.9 ± 3.1	-4.9 ± 3.4

4.2. 3D retrievals and 1D comparisons

Our method of constructing 3D cloud fields was then applied to a subset of this synthetic cloud field. This subsection, shown in Fig. 4.5, was chosen because the cloud field has large variations in terms of cloud inhomogeneity and cloud top heights, introducing substantial levels of illuminating and shadowing for evaluation purposes.

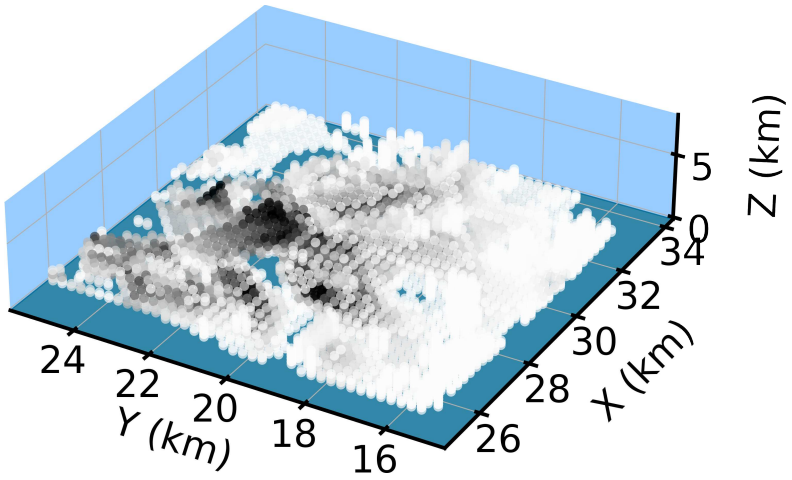

Figure 4.5. Section of synthetic cloud field used to conduct 3D construction. Shown is a 3D scatterplot of each pixel with LWC ≥ 0.01g m^{-3}, with darker colors corresponding to a higher LWC.

The donor-recipient matching process is considerably easier in this context, as there is no uncertainty about the cloud mask of the radar reflectivity profile, all radar reflectivity profiles are usable, and there is no profile contamination due to surface clutter. As discussed in section 3.1.1, all these concerns impacted the DARDAR dataset in our VOCALS-Rex case. Moreover, the viewing and solar geometry is identical for all pixels, removing the uncertainty of how small differences in this geometry can impact observed radiance.

Since the retrieval method under development assumes a constant cloud droplet number concentration (N_c) in each column, we checked whether this assumption was reasonable for the synthetic dataset. Figure 4.6 shows vertical profiles of cloud properties normalized by their column

maximum values; the height is also normalized by their geometric thicknesses, and thus 0 and 1 in the vertical in Fig. 4.6 represent cloud base and cloud top, respectively. These profiles correspond to the 20 most optically thick profiles (Fig. 4.6 (a)) and a selection of 40 random profiles of at least 800 m of geometric thickness (Fig. 4.6 (b)). The thickness condition is to ensure the clouds have enough bins to establish a cloud profile. About half of the optically thick profiles have approximately constant number concentrations and a linear LWC profile. These were largely the only profiles in the field which somewhat consistently had a constant N_d profile. The other half of the most optically thick profiles had a pronounced dip in number concentration, LWC and radar reflectivity. The selection of 40 random profiles has significant variations in the vertical profiles.

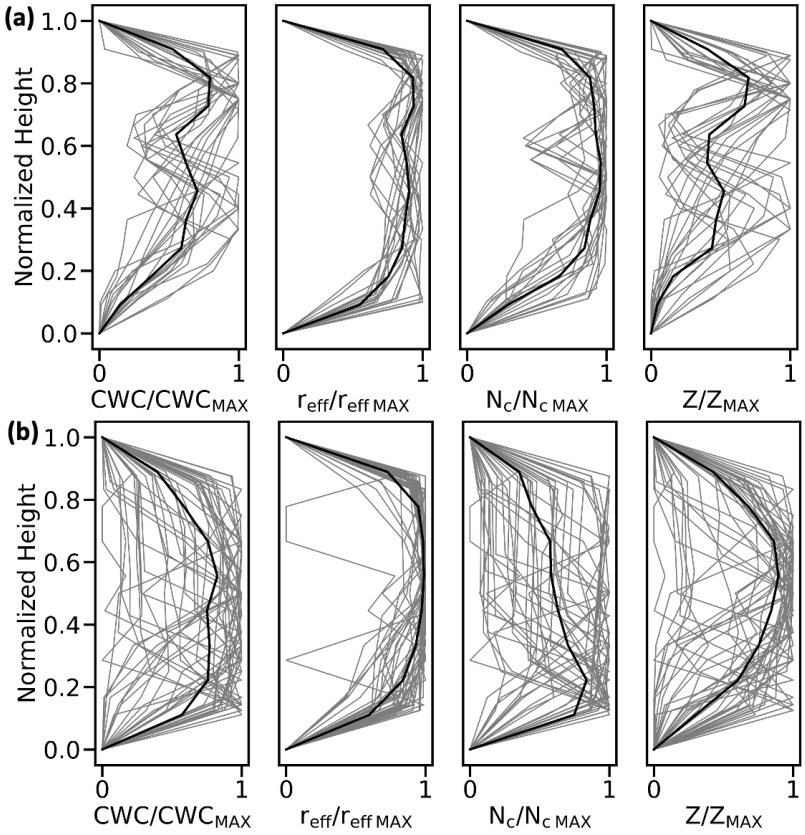

Figure 4.6. Normalized cloud property profiles of cloud water content (CWC), effective radius (r_e), cloud droplet number concentration (N_d), and cloud radar reflectivity (Z) of (a) 20 most optically thick cloud pixels and (b) 40 random cloud profiles at least 800 m thick. This same mean profile structure was observed even when all cloud profiles were included.

In the following example of comparisons, instead of using a constant N_c, the 3D retrieval method used a profile with a shape similar to the intrinsic profile of N_c in Fig. 4.6(a). This allows us to test whether our retrieval method works reasonably if the profile shapes of N_c are not far from the truth. One of the goals of this method was to substantially reduce the errors of retrieved cloud properties when compared to traditional 1D methods. Shown in Fig. 4.7 is a histogram of the absolute errors of those properties compared to the 1D retrieval for those errors. The 1D values are retrieved using the lookup tables as described in Section 4.1. Results show that 3D cloud retrievals are promising, which have more points around the zero line and much fewer error outliers like 1D retrievals. It would be interesting to know how the pixels with significant error reductions in retrievals correlate their illumination and shadowing. Since this example plot is based on a rather small region, further analyses using a larger sample size are needed. The range in retrieved τ errors was reduced from reduced from [–50, 100] to [–30, 40]. The range in retrieved LWP errors was reduced from [–800, 700] to [–250, 300].

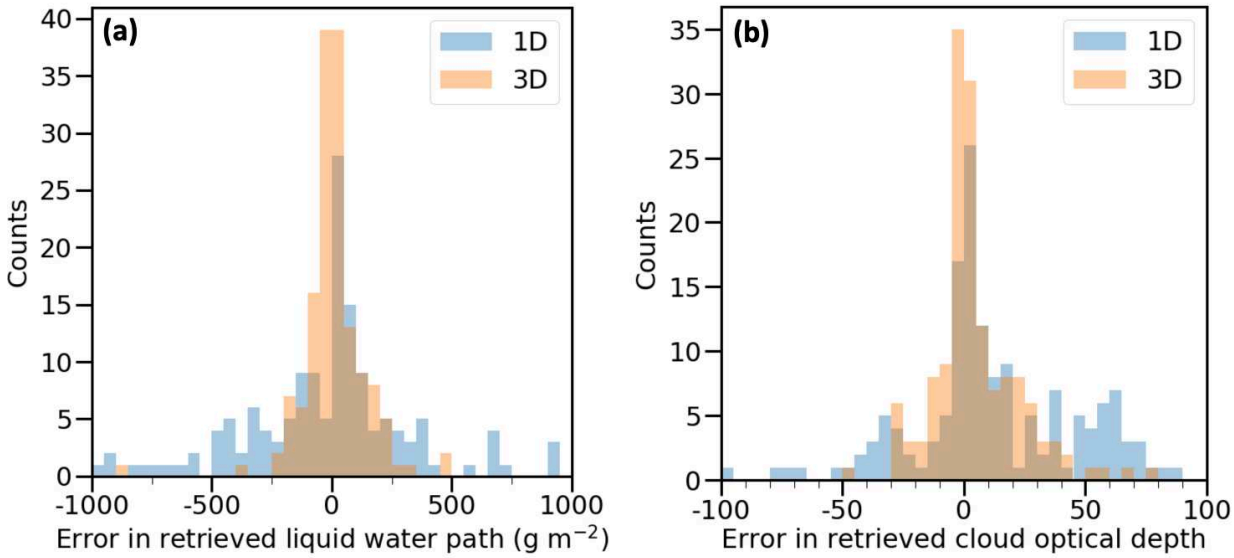

Figure. 4.7. Histogram of errors in retrieved (a) LWP and (b) τ between 1D and our 3D algorithm. Credit: Christine Chiu.

CHAPTER 5: CONCLUSION AND DISCUSSION

5.1. Summary

This thesis sought to construct and evaluate the 3D microphysical properties of stratocumulus cloud fields from passive and active A-train observations for the first time. Improving our observations of these cloud fields is critical, as they are a critical component of the Earth's radiation budget, but are poorly integrated into climate models, as models exhibit a strong radiative flux bias due to a neglect of the 3D effects, which are particularly prevalent among stratocumulus fields (Hogan & Shonk, 2013). Satellite observations are the ideal platform for cloud observations as only they can provide global coverage, but most satellite retrieval methods rely on 1D assumptions, which leads to significant retrieval errors in marine boundary layer clouds. Traditional 1D retrieval methods are especially lacking for stratocumulus clouds, which can overestimate by as much as 100% at oblique solar zenith angles (Zinner & Mayer, 2006).

Constructing 3D cloud fields and incorporating 3D RT allows cloud retrievals to account for the 1D retrieval errors of illumination and shadowing. A past attempt at constructing full 3D microphysical stratocumulus cloud fields from satellite observations by Barker et al. (2011) was required to make significant assumptions about cloud properties and had the key limitations of not being able to determine the uncertainty of the retrieved properties and not incorporating 3D radiative transfer into the retrieval process.

We have developed 3D shortwave radiative transfer emulators for cloud fields which can be used to reduce the substantial computational cost of 3D radiative transfer. Each emulator is specific to a wavelength and set of solar and viewing geometry, and applies to stratocumulus and cumulus cloud regimes. The percent errors of these emulators all have a mean bias of near zero

and standard deviations of as low as 6.6% on low solar zenith angle, viewing nadir cases, and as high as 20% on off-nadir cases, where parallax drives error. However, as consistently achieved 15th and 85th percentile errors of less than ±9% for nearly all setups. By using this emulator in place of radiative transfer via SHDOM, we can significantly reduce the computational cost our method, allowing it to be applied to more real-world satellite observations. This emulator can be used far more broadly than in just this application. As the first emulator of shortwave 3D radiance, this method could be used far more broadly than in just our application. Many remote-sensing applications could use an emulator such as this in a forward model, incorporating 3D radiative effects with a relatively low computational cost.

We also analyzed a potential test case for the implementation of our retrieval on real-world data. The VOCALS-REx field campaign, conducted off the west coast of Chile, provided aircraft data of a stratocumulus cloud deck which coincided with CloudSat and MODIS observations. The cloud field during our selected test flight was subadiabatic, although the N_d profile could be considered reasonably constant with height. This case highlighted the challenges of applying this method to real-world data. Due to surface clutter and limited sensitivity to non-precipitating MBL clouds, CloudSat's CPR was unable to detect substantial portions of the cloud deck due to its low cloud top height, requiring the use of the DARDAR dataset. This also presented problems, as CPR and DARDAR had a poor vertical correlation of cloud observations, and many vertical profiles were missing data, limiting the number of usable donor profiles, which diminishes the accuracy of the method.

When applied to a synthetic cloud field, our 3D retrievals significantly outperformed the traditional IPA retrieval. 1D retrieval had significant errors due to the extent of 3D effects on this cloud field, with LWP errors near 100%. Quantifying the effects of illumination and shadowing

on the 1D retrievals showed that at low solar zenith angles, shadowed pixels had a larger magnitude of mean optical depth bias (–12) than illuminated pixels (3). At high solar zenith angles, the inverse was true; shadowed pixels had a bias of -5 and illuminated pixels had a bias of 12. At a low solar zenith angle, the shift in retrieved effective radius was fairly minimal across shadowed and illuminated pixels compared to a high solar zenith angle. At SZA = 20°, shadowed pixels had a bias of mean 0.8 μm and illuminated pixels had a mean bias of -3.8 μm. We were also able determine that this method of constructing 3D microphysical cloud properties worked even when assumptions about the N_d profile had to be altered. These 3D properties were a significant improvement over 1D-retrieved properties on a tested subset of the synthetic cloud field. Incorporating 3D radiative effects greatly reduced the range of the errors from [–50, 100] to [–30, 40].

Thus, this method is not only an improvement over 1D retrieval methods for 2D properties, but it can determine vertical microphysical property profiles with uncertainty, which no other retrieval method has accomplished. When applied to real-world satellite data, this promises to substantially increase the accuracy of retrieved cloud fields, furthering our understanding of vertical microphysical profiles, which could improve the implementation of stratocumulus clouds into climate models.

5.2. Future work

We have yet to apply this method to real-world data due to the challenges associated with our VOCALS-REx case discussed in Chapter 3. More work is required to allow for a proper comparison of in-situ microphysical properties and the results from our method. However, this case will allow us to determine how our 3D cloud fields perform on real-world data. Next, we can

apply this to more satellite observations of stratocumulus clouds to determine its performance on different types and locations of stratocumulus clouds.

We will also integrate the 3D RT emulator into our retrieval process, which will considerably reduce the required computational cost, making this method more practical to apply to large datasets. As the emulators do not produce the exact solution of 3D RT, this will introduce additional error into the retrieval process, so we will compare the difference in cloud fields produced with the emulators and with SHDOM to assess how much this reduces the accuracy of the retrieved microphysical properties. Our goal is that, even with the additional error, our retrievals will still be significantly more accurate than cloud properties retrieved with 1D methods.

REFERENCES

Andreae, M. O., & Rosenfeld, D. (2008). Aerosol–cloud–precipitation interactions. Part 1. The nature and sources of cloud-active aerosols. Earth-Science Reviews, 89(1–2), 13–41. https://doi.org/10.1016/j.earscirev.2008.03.001

Barker, H. W., Jerg, M. P., Wehr, T., Kato, S., Donovan, D. P., & Hogan, R. J. (2011). A 3D cloud-construction algorithm for the EarthCARE satellite mission. Quarterly Journal of the Royal Meteorological Society, 137(657), 1042–1058. https://doi.org/10.1002/qj.824

Bony, S., & Dufresne, J.-L. (2005). Marine boundary layer clouds at the heart of tropical cloud feedback uncertainties in climate models. Geophysical Research Letters, 32(20), L20806. https://doi.org/10.1029/2005GL023851

Cai, Y., Snider, J. R., & Wechsler, P. (2013). Calibration of the passive cavity aerosol spectrometer probe for airborne determination of the size distribution. Atmospheric Measurement Techniques, 6(9), 2349–2358. https://doi.org/10.5194/amt-6-2349-2013

Cazenave, Q., Ceccaldi, M., Delanoë, J., Pelon, J., Groß, S., & Heymsfield, A. (2019). Evolution of DARDAR-CLOUD ice cloud retrievals: New parameters and impacts on the retrieved microphysical properties. Atmospheric Measurement Techniques, 12(5), 2819–2835. https://doi.org/10.5194/amt-12-2819-2019

Chen, T., Rossow, W. B., & Zhang, Y. (2000). Radiative Effects of Cloud-Type Variations. Journal of Climate, 13(1), 264–286. https://doi.org/10.1175/1520-0442(2000)013<0264:REOCTV>2.0.CO;2

Evans, K. F. (1998). The Spherical Harmonics Discrete Ordinate Method for Three-Dimensional Atmospheric Radiative Transfer. Journal of the Atmospheric Sciences, 55(3), 429–446. https://doi.org/10.1175/1520-0469(1998)055<0429:TSHDOM>2.0.CO;2

Fielding, M. D., Chiu, J. C., Hogan, R. J., & Feingold, G. (2014). A novel ensemble method for retrieving properties of warm cloud in 3-D using ground-based scanning radar and zenith radiances: Retrieving 3D cloud properties. Journal of Geophysical Research: Atmospheres, 119(18), 10,912-10,930. https://doi.org/10.1002/2014JD021742

Fielding, M. D., Chiu, J. C., Hogan, R. J., Feingold, G., Eloranta, E., O'Connor, E. J., & Cadeddu, M. P. (2015). Joint retrievals of cloud and drizzle in marine boundary layer clouds using ground-based radar, lidar and zenith radiances. Atmospheric Measurement Techniques, 8(7), 2663–2683. https://doi.org/10.5194/amt-8-2663-2015

Haynes, J. M., Marchand, R. T., Luo, Z., Bodas-Salcedo, A., & Stephens, G. L. (2007). A Multipurpose Radar Simulation Package: QuickBeam. Bulletin of the American Meteorological Society, 88(11), 1723–1728. https://doi.org/10.1175/BAMS-88-11-1723

Hersbach, H., Bell, B., Berrisford, P., Hirahara, S., Horányi, A., Muñoz-Sabater, J., Nicolas, J., Peubey, C., Radu, R., Schepers, D., Simmons, A., Soci, C., Abdalla, S., Abellan, X., Balsamo, G., Bechtold, P., Biavati, G., Bidlot, J., Bonavita, M., … Thépaut, J. (2020). The ERA5 global reanalysis. Quarterly Journal of the Royal Meteorological Society, 146(730), 1999–2049. https://doi.org/10.1002/qj.3803

Hu, X., Ge, J., Li, Y., Marchand, R., Huang, J., & Fu, Q. (2020). Improved Hydrometeor Detection Method: An Application to CloudSat. Earth and Space Science, 7(2). https://doi.org/10.1029/2019EA000900

Jakub, F., & Mayer, B. (2015). A three-dimensional parallel radiative transfer model for atmospheric heating rates for use in cloud resolving models—The TenStream solver. Journal of Quantitative Spectroscopy and Radiative Transfer, 163, 63–71. https://doi.org/10.1016/j.jqsrt.2015.05.003

Jia, H., Ma, X., & Liu, Y. (2019). Exploring aerosol–cloud interaction using VOCALS-REx aircraft measurements. Atmospheric Chemistry and Physics, 19(12), 7955–7971. https://doi.org/10.5194/acp-19-7955-2019

King, W. D., Parkin, D. A., & Handsworth, R. J. (1978). A Hot-Wire Liquid Water Device Having Fully Calculable Response Characteristics. Journal of Applied Meteorology, 17(12), 1809–1813. https://doi.org/10.1175/1520-0450(1978)017<1809:AHWLWD>2.0.CO;2

Kostka, P. M., Weissmann, M., Buras, R., Mayer, B., & Stiller, O. (2014). Observation Operator for Visible and Near-Infrared Satellite Reflectances. Journal of Atmospheric and Oceanic Technology, 31(6), 1216–1233. https://doi.org/10.1175/JTECH-D-13-00116.1

Leinonen, J., Guillaume, A., & Yuan, T. (2019). Reconstruction of Cloud Vertical Structure With a Generative Adversarial Network. Geophysical Research Letters, 46(12), 7035–7044. https://doi.org/10.1029/2019GL082532

Liang, X., Garrett, K., Liu, Q., Maddy, E. S., Ide, K., & Boukabara, S. (2022). A Deep-Learning-Based Microwave Radiative Transfer Emulator for Data Assimilation and Remote Sensing. IEEE Journal of Selected Topics in Applied Earth Observations and Remote Sensing, 15, 8819–8833. https://doi.org/10.1109/JSTARS.2022.3210491

Marchand, R., Mace, G. G., Ackerman, T., & Stephens, G. (2008). Hydrometeor Detection Using Cloudsat—An Earth-Orbiting 94-GHz Cloud Radar. Journal of Atmospheric and Oceanic Technology, 25(4), 519–533. https://doi.org/10.1175/2007JTECHA1006.1

Marshak, A., Platnick, S., Várnai, T., Wen, G., & Cahalan, R. F. (2006). Impact of three-dimensional radiative effects on satellite retrievals of cloud droplet sizes. Journal of Geophysical Research, 111(D9), D09207. https://doi.org/10.1029/2005JD006686

Martin, M., Ghent, D., Pires, A., Göttsche, F.-M., Cermak, J., & Remedios, J. (2019). Comprehensive In Situ Validation of Five Satellite Land Surface Temperature Data Sets over Multiple Stations and Years. Remote Sensing, 11(5), 479. https://doi.org/10.3390/rs11050479

Mason, S. L., Hogan, R. J., Bozzo, A., & Pounder, N. L. (2022). A unified synergistic retrieval of clouds, aerosols and precipitation from EarthCARE: The ACM-CAP product [Preprint]. Clouds/Remote Sensing/Data Processing and Information Retrieval. https://doi.org/10.5194/egusphere-2022-1195

Mechoso, C. R., Wood, R., Weller, R., Bretherton, C. S., Clarke, A. D., Coe, H., Fairall, C., Farrar, J. T., Feingold, G., Garreaud, R., Grados, C., McWilliams, J., de Szoeke, S. P., Yuter, S. E., & Zuidema, P. (2014). Ocean–Cloud–Atmosphere–Land Interactions in the Southeastern Pacific: The VOCALS Program. Bulletin of the American Meteorological Society, 95(3), 357–375. https://doi.org/10.1175/BAMS-D-11-00246.1

Nakajima, T., & King, M. D. (1990). Determination of the Optical Thickness and Effective Particle Radius of Clouds from Reflected Solar Radiation Measurements. Part I: Theory. Journal of the Atmospheric Sciences, 47(15), 1878–1893. https://doi.org/10.1175/1520-0469(1990)047<1878:DOTOTA>2.0.CO;2

Painemal, D., & Zuidema, P. (2011). Assessment of MODIS cloud effective radius and optical thickness retrievals over the Southeast Pacific with VOCALS-REx in situ measurements: MODIS VALIDATION DURING VOCALS-REx. Journal of Geophysical Research: Atmospheres, 116(D24), n/a-n/a. https://doi.org/10.1029/2011JD016155

Pan, B., Liu, D., Kumar, K. R., Wang, M., & Devi, N. S. M. P. L. (2021). Global distribution of maritime low clouds with an emphasis on different aerosol types and meteorological

parameters inferred from multi-satellite and reanalysis data during 2007–2016. Atmospheric Environment, 246, 118082. https://doi.org/10.1016/j.atmosenv.2020.118082

Patadia, F., Levy, R. C., & Mattoo, S. (2018). Correcting for trace gas absorption when retrieving aerosol optical depth from satellite observations of reflected shortwave radiation. Atmospheric Measurement Techniques, 11(6), 3205–3219. https://doi.org/10.5194/amt-11-3205-2018

Platnick, S., Ackerman, S., & King, M. D. (2015). MODIS Atmosphere L2 Cloud Product (06_L2) [Data set]. NASA MODIS Adaptive Processing System, Goddard Space Flight Center, USA. https://doi.org/10.5067/MODIS/MOD06_L2.006

Remer, L., Tanre, D., & Kaufman, Y. (2009). ALGORITHM FOR REMOTE SENSING OF TROPOSPHERIC AEROSOL FROM MODIS: Collection 5. NASA MODIS Adaptive Processing System, Goddard Space Flight Center, USA. https://modis.gsfc.nasa.gov/data/atbd/atbd_mod02.pdf

Stamnes, K., Tsay, S.-C., Wiscombe, W., & Jayaweera, K. (1988). Numerically stable algorithm for discrete-ordinate-method radiative transfer in multiple scattering and emitting layered media. Applied Optics, 27(12), 2502. https://doi.org/10.1364/AO.27.002502

Stephens, G. L., Vane, D. G., Boain, R. J., Mace, G. G., Sassen, K., Wang, Z., Illingworth, A. J., O'connor, E. J., Rossow, W. B., Durden, S. L., Miller, S. D., Austin, R. T., Benedetti, A., Mitrescu, C., & the CloudSat Science Team. (2002). THE CLOUDSAT MISSION AND THE A-TRAIN: A New Dimension of Space-Based Observations of Clouds and Precipitation. Bulletin of the American Meteorological Society, 83(12), 1771–1790. https://doi.org/10.1175/BAMS-83-12-1771

Vaughan, M. A., Powell, K. A., Winker, D. M., Hostetler, C. A., Kuehn, R. E., Hunt, W. H., Getzewich, B. J., Young, S. A., Liu, Z., & McGill, M. J. (2009). Fully Automated Detection of Cloud and Aerosol Layers in the CALIPSO Lidar Measurements. Journal of Atmospheric and Oceanic Technology, 26(10), 2034–2050. https://doi.org/10.1175/2009JTECHA1228.1

Werkmeister, A., Lockhoff, M., Schrempf, M., Tohsing, K., Liley, B., & Seckmeyer, G. (2015). Comparing satellite- to ground-based automated and manual cloud coverage observations – a case study. Atmospheric Measurement Techniques, 8(5), 2001–2015. https://doi.org/10.5194/amt-8-2001-2015

Werner, F., Zhang, Z., Wind, G., Miller, D. J., Platnick, S., & Di Girolamo, L. (2018). Improving Cloud Optical Property Retrievals for Partly Cloudy Pixels Using Coincident Higher-Resolution Single Band Measurements: A Feasibility Study Using ASTER Observations. Journal of Geophysical Research: Atmospheres, 123(21). https://doi.org/10.1029/2018JD028902

Winker, D. M., Hunt, W. H., & McGill, M. J. (2007). Initial performance assessment of CALIOP. Geophysical Research Letters, 34(19), L19803. https://doi.org/10.1029/2007GL030135

Winker, D. M., Pelon, J., Coakley, J. A., Ackerman, S. A., Charlson, R. J., Colarco, P. R., Flamant, P., Fu, Q., Hoff, R. M., Kittaka, C., Kubar, T. L., Le Treut, H., Mccormick, M. P., Mégie, G., Poole, L., Powell, K., Trepte, C., Vaughan, M. A., & Wielicki, B. A. (2010). The CALIPSO Mission. Bulletin of the American Meteorological Society, 91(9), 1211–1230. https://doi.org/10.1175/2010BAMS3009.1

Wood, R. (2012). Stratocumulus Clouds. Monthly Weather Review, 140(8), 2373–2423. https://doi.org/10.1175/MWR-D-11-00121.1

Zheng, X., Albrecht, B., Jonsson, H. H., Khelif, D., Feingold, G., Minnis, P., Ayers, K., Chuang, P., Donaher, S., Rossiter, D., Ghate, V., Ruiz-Plancarte, J., & Sun-Mack, S. (2011). Observations of the boundary layer, cloud, and aerosol variability in the southeast Pacific near-coastal marine stratocumulus during VOCALS-REx. Atmospheric Chemistry and Physics, 11(18), 9943–9959. https://doi.org/10.5194/acp-11-9943-2011

Zinner, T., and Mayer, B. (2006). Remote Sensing of Stratocumulus Clouds: Uncertainties and Biases Due to Inhomogeneity. Journal of Geophysical Research, 11(D14). https://doi.org/10.1029/2005JD006955